TEKTONIKA

Structural Control of Fluid Circulation and Permeability in Active Transpression Along and Adjacent to the Bartlett Springs Fault, Northern California Coast Ranges

Benjamin L. Melosh *[1], **Owen A. Callahan** [2]

[1]U.S. Geological Survey, Moffett Field, CA 94035, USA | [2]En Échelon Geosolutions, Palo Alto, CA 94306, USA

Abstract Localized zones of extension in transpressional fault systems can create open fractures that act as conduits for geothermal fluids. Structurally controlled fluid pathways are well documented in extensional and transtensional settings; however, their presence and role in contractional or transpressional settings remain under-recognized. In this paper, we investigate the structural control of fluid flow along the right-lateral Bartlett Springs Fault in the Coast Ranges of northern California. We combine new geothermometry, thermal mapping, and dilation tendency analysis with published bedrock geologic mapping and stress inversions to present a new conceptual model highlighting various structural controls of fluid flow, including appropriately oriented secondary faults and fractures in an antiformal hinge zone. In the modern stress field, the Bartlett Springs Fault itself is a statically closed fluid barrier that hosts only shallowly circulating warm springs. East of the fault, in the hinge of the Quaternary-active Wilbur Springs antiform, northeast- and northwest-striking strike-slip and oblique-normal faults intersect at a high angle, with fault intersections that plunge steeply to depth. Northeast-striking faults are subparallel to the maximum horizontal stress and have high dilation tendency, creating possible fluid pathways along open fractures and fault intersections. Hot springs with the highest-temperature geothermometry and thermal imagery results coincide with the hinge of the Wilbur Springs antiform, where extensional deformation is expected to be highest, allowing for additional fluid pathways and circulation. This work demonstrates that fluid circulation occurs in areas of local extension within transpressional settings, and the spatial overlap of multiple fluid-pathway-generating mechanisms provides favorable conditions for upwelling of geothermal fluids.

Executive Editor:
Craig Magee
Associate Editor:
Frank Zwaan
Technical Editor:
Mohamed Gouiza

Reviewers:
Adam Cawood
Åke Fagereng

Submitted:
5 June 2025
Accepted:
9 October 2026
Published:
26 November 2026

1 Introduction

Geometric irregularities along fault zones play a critical role in controlling fluid flow and deep fluid circulation by localizing stress concentrations and enhancing permeability (e.g., *Curewitz and Karson*, 1997; *Rowland and Sibson*, 2004; *Faulds and Hinz*, 2014). Irregularities such as bends, jogs, and step-overs influence mechanical behavior and deformation patterns over a variety of strain rates, including during earthquakes (e.g., *Sibson*, 1994; *Faulds and Hinz*, 2014). As fault displacement progresses, these structural complexities can create transient openings and localized dilational zones that may facilitate the migration and circulation of fluids (e.g., *Siler et al.*, 2018; *Siler*, 2023). This can occur in the mid-crust at elevated strain rates, where transient permeability variations and dynamic stress changes influence deep-seated fluid transport (*Melosh et al.*, 2016). Fault opening may compete with mineral precipitation and fault healing or local zones of shortening at restraining bends that act to close faults and occlude fractures, reducing permeability (*Sibson*, 1996). Therefore, to understand fluid flow, it is essential to identify which structures are mechanically predisposed to remain open. The effects of fault zone processes and fluid flow are observed both in exhumed fault systems (*Caine et al.*, 2010; *Callahan et al.*, 2019) and in active geothermal and tectonic settings (e.g., *Pluhar et al.*, 2006; *Anderson and Fairley*, 2008; *Siler et al.*, 2018), highlighting the fundamental role of fault geometry in governing crustal-scale fluid dynamics.

The relationships between fault geometry and fluid upwelling are well documented in extensional settings, particularly within the Basin and Range province of the western United States, where crustal extension promotes enhanced permeability and vertical fluid migration (e.g., *Curewitz and Karson*, 1997; *Faulds and Hinz*, 2014). In these regions, specific fault geometries such as releasing bends, releasing step-overs, terminations, accommodation zones, and fault intersections act as primary conduits for geothermal fluids, facilitating hydrothermal circulation and the

*✉ bmelosh@usgs.gov

formation of geothermal reservoirs (e.g., *Faulds et al.*, 2005; *Faulds and Hinz*, 2014). Similar structural controls have been identified along strike-slip faults, where transtensional irregularities create high-permeability pathways for fluid circulation, focusing hydrothermal upwelling (e.g., *Muraoka et al.*, 2010; *Libbey et al.*, 2015; *Barcelona et al.*, 2019). Localized dilational zones enhance fracture permeability, allowing deep-seated fluids to ascend toward the surface, reducing the effective normal stress.

The association between active strike-slip faulting and geothermal fluid flow is well exemplified by The Geysers geothermal field in the Coast Ranges of northern California, within the broader San Andreas transform system. The Geysers are situated within a transtensional zone bounded by several major strike-slip faults, including the Collayomi Fault to the east and the Geyser Peak, Mercuryville, and Maacama faults to the west (Figure 1; *McLaughlin*, 1981a; *Stanley et al.*, 1997, 1998; *Melosh*, 2026). *Stanley et al.* (1997) postulated that this zone of transtension extends about 30 km farther northeast to the Bartlett Springs Fault and may have allowed for the ascent of the Geysers Plutonic Complex, which was emplaced between 1.8 and 1.1 Ma (*Schmitt et al.*, 2003).

Within a single geothermal field there may be zones of tension and compression, such as a fault termination or a restraining bend in an otherwise transtensional strike-slip fault system. However, the importance of subsurface fluid flow is often overlooked in shortening and transpressional settings (e.g., *Evans and Fischer*, 2012; *Maffucci et al.*, 2016), despite the importance of these environments in active hydrothermal and analogous mineralizing systems (e.g., *Sibson et al.*, 1988; *Robert and Poulsen*, 2001). The generation and growth of fold sets can shape fluid flow pathways and exert critical control over hydrothermal systems by the interplay between tensile stresses in fold hinges, mechanical interactions within folded layers, and the development of joint sets or secondary faults (e.g., *Evans and Fischer*, 2012). Given these complexities, a more detailed investigation into fluid upwelling in compressional settings could advance our understanding of geothermal potential and fluid-rock interactions.

In this paper, we investigate the structural controls on fluid flow along the strike-slip Bartlett Springs Fault Zone (BSF) and the adjacent Wilbur Springs antiform in the Coast Ranges of northern California (Figure 1). The concentration of springs along the Bartlett Springs Fault suggests that the fault zone exerts a primary structural control on fluid ascent and circulation. Our study focuses on the 30-km segment between Crabtree Hot Springs and Wilson Valley, and includes Wilbur Springs on the east side of the BSF in an area of predicted transpressional strain (*Melosh*, 2026). We hypothesize that fluid circulation in the Wilbur Springs area is not controlled by a single structure, but rather by the confluence of three specific mechanical factors: (1) localized tensile stresses developed within the hinges of active antiforms, (2) the presence of secondary faults with high dilation tendency relative to the regional stress field, and (3) the formation of high-permeability conduits at steeply plunging fault intersections. By integrating geothermometry with dilation tendency analysis, we test whether the spatial overlap of these mechanisms creates the permeability necessary for high-temperature upwelling in an otherwise contractional regime.

2 Background

2.1 The Bartlett Springs Fault (BSF)

The BSF zone is a ∼170-km-long, right-lateral strike-slip fault zone capable of producing $M_w > 7$ earthquakes (*Lozos et al.*, 2015). The fault is part of the broader San Andreas Fault System in the Coast Ranges of northern California (Figure 1), and its northwest strike is subparallel to the structural grain of the bedrock (*Mclaughlin et al.*, 2018). The fault geometry includes local releasing step-overs, fault bends, and multiple interconnected fault strands (*Lienkaemper*, 2010). A large releasing step-over at Lake Pillsbury, 12 km north of the study area (Figure 1), localizes the vertical ascent of antigorite serpentine from depth (*Moore et al.*, 2018). Microseismicity clusters suggest the fault dips steeply east (*Mclaughlin et al.*, 2018), and aeromagnetic anomalies indicate a substantial amount of serpentinite in the subsurface (*Langenheim et al.*, 2024). At Wilson Valley, the BSF forms a releasing step-over approximately 3 km wide and connects with the Hunting Creek Fault strand of the southern part of the BSF, which continues south out of the current study area (Figure 1; *Lienkaemper*, 2010; *Melosh et al.*, 2024a).

The geology surrounding the BSF in the study area is varied and complex (Figure 2) and primarily consists of blueschist-grade graywackes and tectonically interleaved block-in-matrix mélange of the Eastern Belt of the Franciscan Complex, fault-bounded slivers of serpentinite of the Coast Range ophiolite, and the Great Valley group, which includes an ophiolitic block mélange tectonically entrained within the fault zone (Figure 2; e.g., *McLaughlin et al.*, 1990; *Mclaughlin et al.*, 2018; *Melosh et al.*, 2024a). *Mclaughlin et al.* (2018) recognized the presence of several large antiform-synform pairs along the BSF including the Wilbur Springs antiform, which is located northeast of the BSF in the study area (Figure 2). They interpreted these folds as having formed during active transpressional deformation on this part of the BSF.

Other faults of note in the study area, adjacent to the BSF, are the Cross Springs Fault and the Little Indian Valley Fault Zone (LIVFZ; Figures 1, 2). The Cross Springs Fault is a ∼20-km-long, steeply east-dipping normal fault that branches off the BSF and is curvilinear, changing strike from northwest to northeast (*McLaughlin et al.*, 1990). The fault bounds the gravels of the Cache Formation (QTc) on the west and hosts a cluster of five warm springs (Figure 2; *Thompson et al.*, 1981). The LIVFZ branches from the BSF in a west-northwest–east-southeast orientation. The fault zone includes older thrust fault contacts

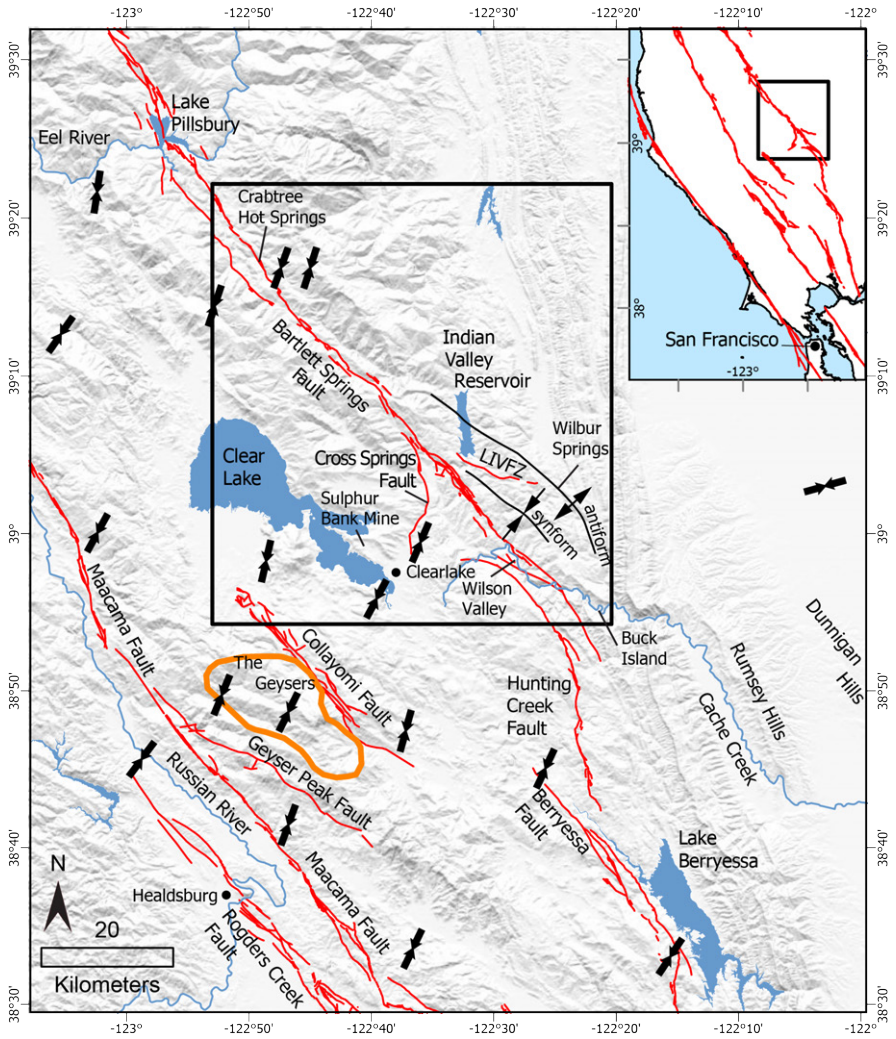

Figure 1 – The location of the study area in the Coast Ranges of northern California and local geographical features and faults. The inset map at the top right shows the position of the study area in the black box in relation to the San Andreas Fault System (shown in red) (*U.S. Geological Survey*, 2004) in the northern Coast Ranges, north of San Francisco, California. The hillshade map (*Esri*, 2015) provides an overview of local fault zones in and surrounding the study area (black box). Population centers, faults, water bodies, and local geographic features mentioned in the text are labeled. Inclined bold black arrows are stress inversion locations from *Provost and Houston* (2003) showing the orientation of maximum horizontal stress. The orange polygon represents The Geysers geothermal field. LIVFZ: Little Indian Valley Fault Zone.

between the Coast Range ophiolite and surrounding Great Valley group sedimentary rocks (*McLaughlin et al.*, 1990). Quaternary traces of the LIVFZ (*U.S. Geological Survey*, 2004) and the nearby Resort Fault have "poor" certainty and thus are shown as dashed and queried in Figure 2 and were not included in the dilation tendency analysis.

A previous stress inversion study reveals an average maximum horizontal stress direction (S_{Hmax}) in the northern Coast Ranges of N26°E (Figure 1; *Provost and Houston*, 2003). This is a strike-slip setting, and we assume S_{Hmax} is the maximum principal stress. The orientation of S_{Hmax} is approximately 75° from the average orientation of the BSF in the study area, and imposes transpressional strain on the fault (Figure 1). Despite this, numerous springs are found along the BSF, indicating structural control on fluid flow (Figure 2). Notably, no springs are present within the dilational step-over at Wilson Valley (Figure 1); instead, fluid discharge occurs farther northeast at Wilbur Springs, suggesting a different structural mechanism may be influencing fluid migration in this region.

2.2 Geology and Neotectonics of Wilbur Springs

The geology of Wilbur Springs was mapped by *McLaughlin et al.* (1990); *Mclaughlin et al.* (2018), although mapping as early as *Lawton* (1956) delineated an antiformal structure in the Wilbur Springs area. The Wilbur Springs antiform deforms sedimentary rocks of the lower Great Valley group, serpentinite of the Coast Range ophiolite, and contains Eastern Belt metagraywackes in its core near Little Indian Valley Reservoir (Figures 2, 3; *Mclaughlin et al.*, 2018). The antiform trends ~130° and plunges gently to the southeast (*Mclaughlin et al.*, 2018), roughly perpendicular to the maximum horizontal stress direction from stress inversions (*Provost and Houston*, 2003). *McLaughlin et al.* (1990) mapped a network of short, but interconnected, oblique normal faults,

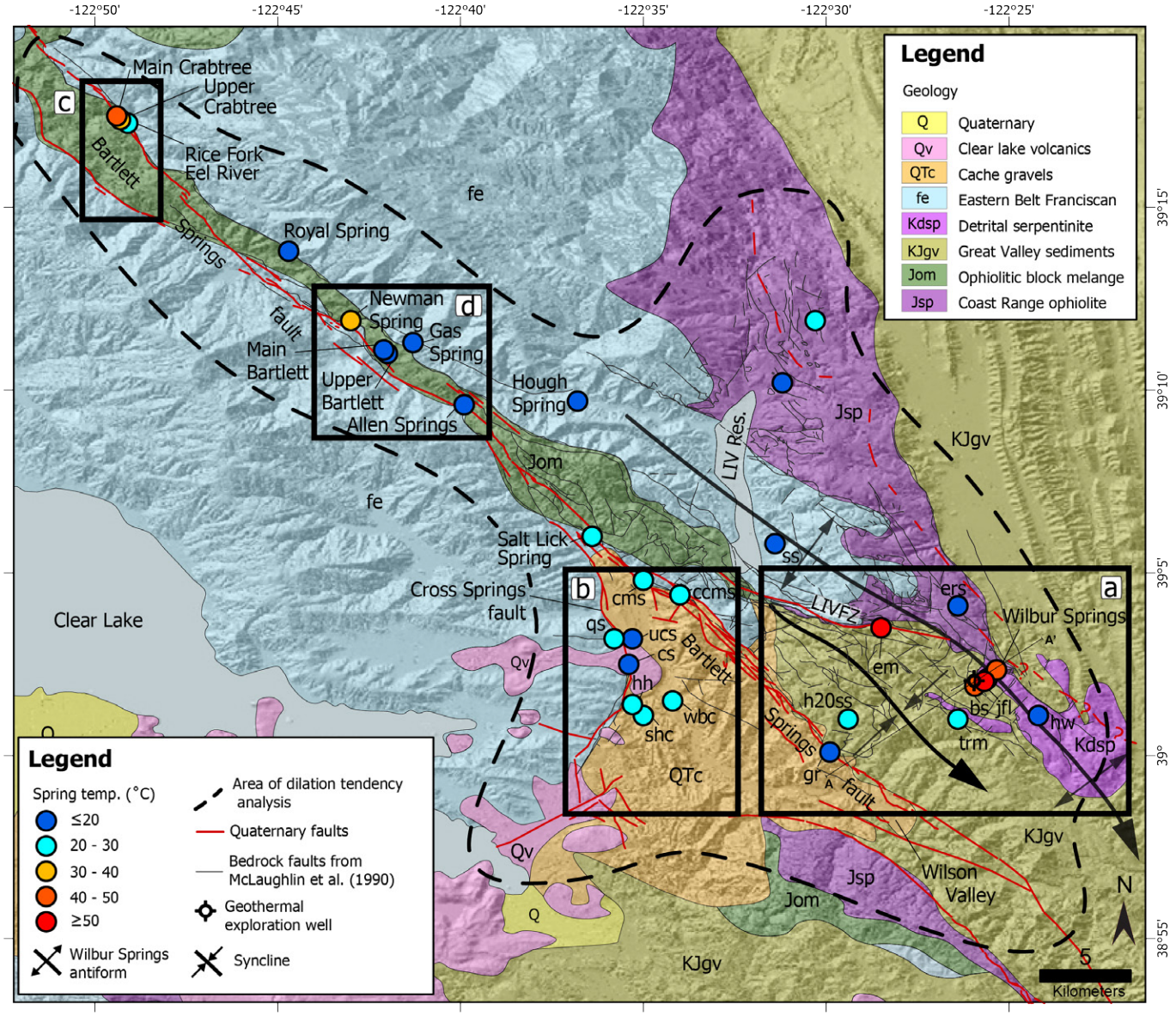

Figure 2 – Spring locations and geology along the Bartlett Springs Fault and surrounding area. Springs used in this study (n = 30) were sampled and located by *Thompson et al.* (1981). Black boxes labeled a–d are focus areas of the dilation tendency analysis. The geology and the position of the Wilbur Springs antiform-synform pair are compiled from *Mclaughlin et al.* (2018) and overlain on a lidar hillshade (*U.S. Geological Survey*, 2018). The thick black dashed line is the boundary of the dilation tendency analysis; Quaternary faults are shown in red (*U.S. Geological Survey*, 2004) and thin black faults are bedrock faults from previous geologic maps. Spring abbreviations include jfl: Jones Fountain of Life Spring, bs: Blank Spring, trm: Turkey Run Mine, tcw: Toby's Cold Well, h20ss: Highway 20 Sulfur Spring, ccms: Cache Creek Magnesite Spring, cms: Chalk Mountain Spring, ucs: Unnamed Cold Spring, cs: Cross Spring, wbc: Well in Benmore Canyon, shc: Spring in Sweet Hollow Creek. LIV Res.: Little Indian Valley Reservoir. The trace of cross section A–A′ is indicated by the thin black line.

located south of the LIVFZ and east of the BSF, near the axial trace of the Wilbur Springs antiform (Figure 3). These northeast- or northwest-striking fault sets intersect at high angles and dip between 50° and 80°; where visible, kinematic indicators suggest oblique-normal-sense motion (*McLaughlin et al.*, 1990).

A geophysical model in the Wilbur Springs area based on aeromagnetic and geologic datasets reveals that serpentinite is folded in the subsurface between depths of ∼2.5 and 5 km (Figure 3b; see cross section 11 in *Langenheim et al.*, 2024). The position of fold hinges at depth, suggested by peaks in the aeromagnetic data, coincides with mapped fold hinges at the surface (e.g., *McLaughlin et al.*, 1990). Overall, *Langenheim et al.* (2024) found more serpentinite in the subsurface surrounding the BSF than expected from what is exposed at the surface. Serpentinite may weaken the BSF and act as a low-permeability fluid barrier in and surrounding the fault zone and below Wilbur Springs.

Uplifted river terraces on Cache Creek (*Gaines*, 2008), including terraces offset by faults in Wilson Valley (*Lienkaemper et al.*, 2014) and Buck Island (Figure 1; *Melosh et al.*, 2024a), attest to ongoing uplift and faulting on the eastern edge of the northern Coast Ranges. At Wilbur Springs, uplift is suggested by an elevated river terrace near the antiformal hinge (Figure 4). The Wilbur Springs antiform trends to the south-southeast where it merges with a broader fold belt

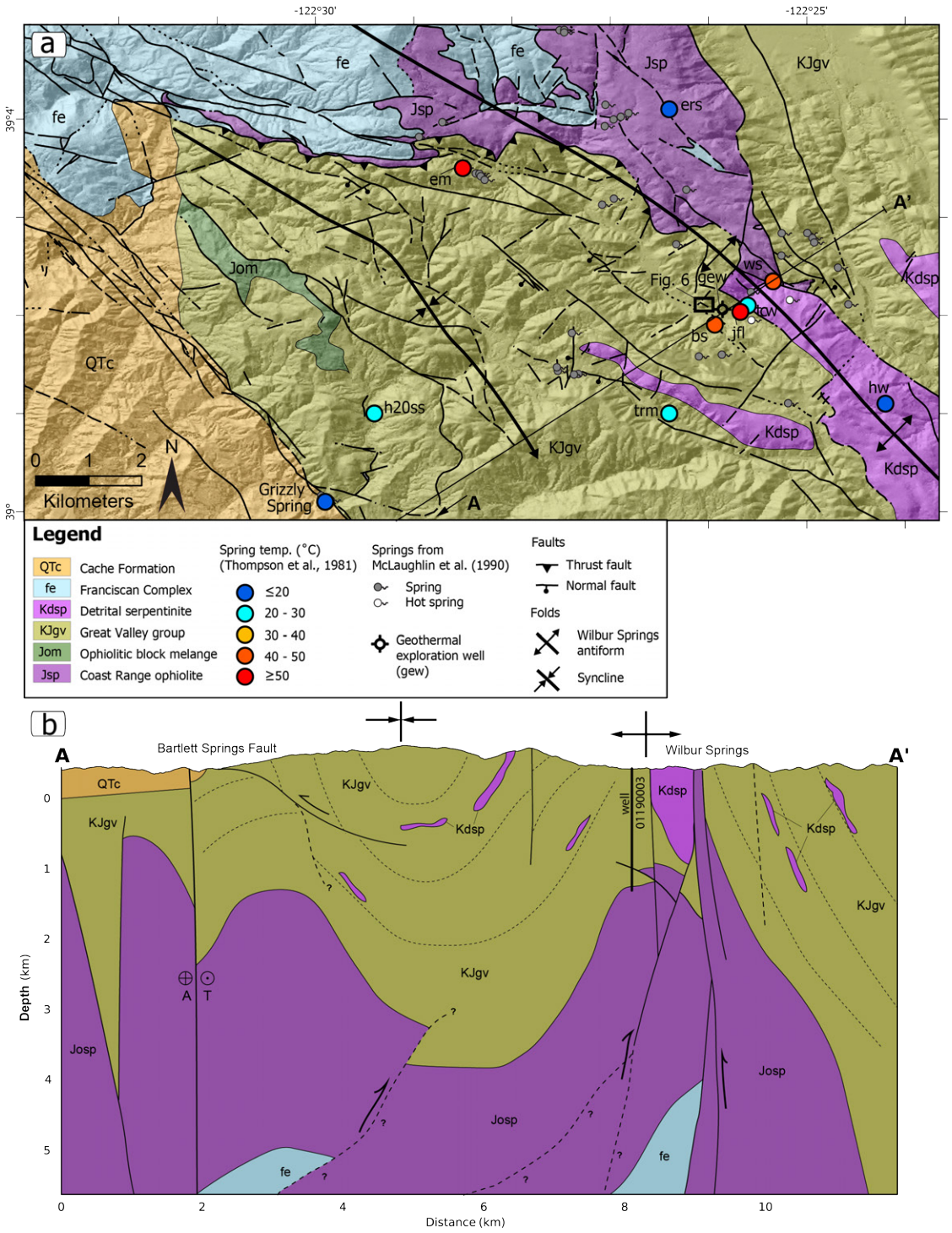

Figure 3 – Surface and subsurface geology of the Wilbur Springs area. a) Geologic map compiled from *McLaughlin et al.* (1990) and *Mclaughlin et al.* (2018), corresponding to box a in Figure 2. Black lines are the fault network used in the dilation tendency analysis compiled from geologic maps and the Quaternary fault database (*U.S. Geological Survey*, 2004). The location of the exploration geothermal well is from *California Division of Oil, Gas, and Geothermal Resources* (2024). Spring location and temperature data are cited in the legend. Spring name abbreviations are ws: Wilbur Springs, bs: Blank Spring, jfl: Jones Fountain of Life Spring, em: Elgin Mine, tcw: Toby's Cold Well, ers: Eagle Rock Spring, hw: Hayfield Well, trm: Turkey Run Mine, h20ss: Highway 20 Sulfur Spring. The location of Figure 5 is marked by the small black box. b) Geologic cross section of the Wilbur Springs area based on surface geologic mapping, seismic profile "Shell Line 806" (*Constenius et al.*, 2000), geothermal exploration Sunoco well 01190003 (*California Division of Oil, Gas, and Geothermal Resources*, 2024), and aeromagnetic and gravity datasets (*Langenheim et al.*, 2024). The location of cross section A–A′ is indicated by the thin black line on the geologic map and is oriented approximately perpendicular to the Wilbur Springs antiform. The folded serpentinite geometry is primarily derived from the aeromagnetic data inversion as well as bottomhole lithology from well 01190003; deep fault geometry is queried from subsurface interpretations of *McLaughlin et al.* (1990) and faults interpreted from the seismic profile (*Constenius et al.*, 2000). No vertical exaggeration. A: Away, T: Toward. Thin, short dashed lines in unit KJgv indicate approximate bedding orientations.

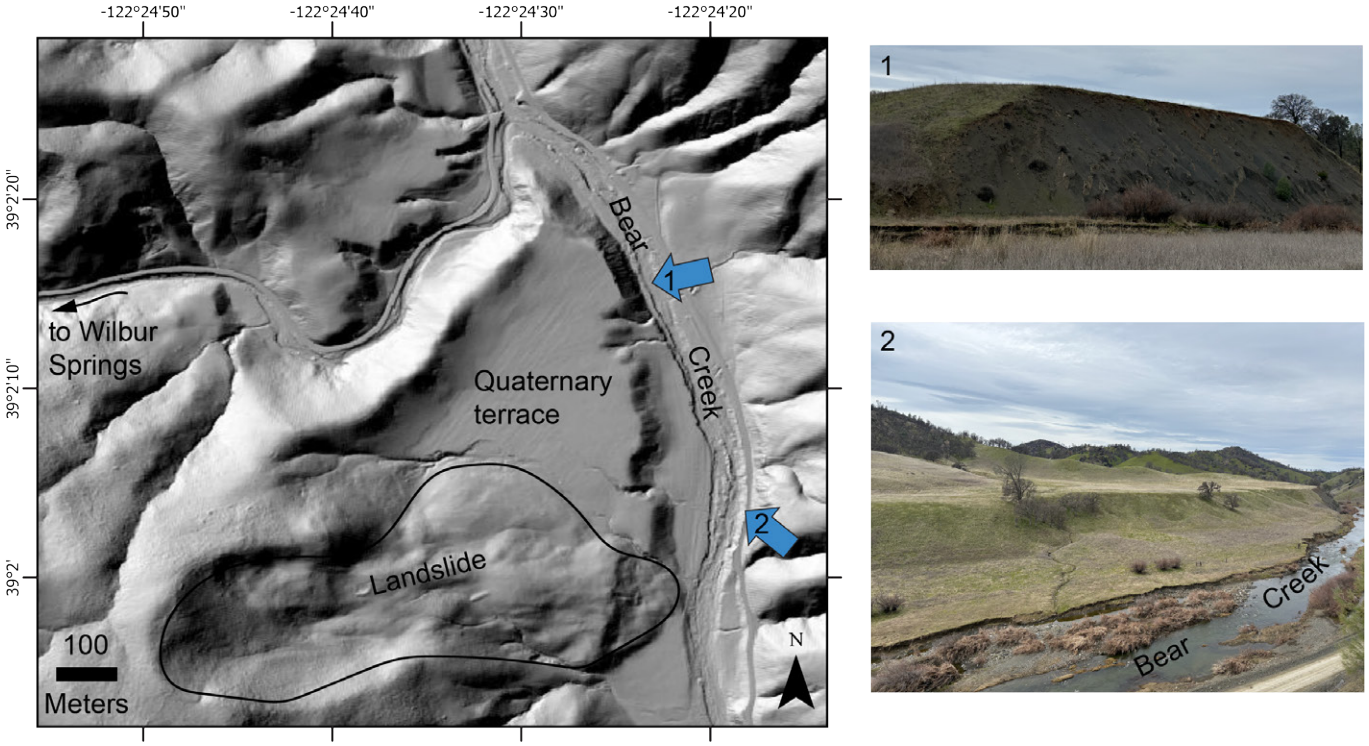

Figure 4 – Lidar map and field photographs showing location of an elevated river terrace ∼1 km east of Wilbur Springs. Blue numbered arrows are the locations and directions of the photographs shown on the right. One-meter-resolution lidar data are from *U.S. Geological Survey* (2018); photographs by Ben Melosh, U.S. Geological Survey, 2025.

that underlies river terraces along Cache Creek (*Melosh et al.*, 2024a). It is possible that a component of active uplift is driven by folding.

GPS velocity inversion studies find that the BSF experiences shortening of up to 2.9 mm/yr, with a preferred rate with geologic constraints of 1.1 mm/yr (*Zeng and Shen*, 2014). Shortening drives east–west-directed dip-slip displacement and uplift on faults along the eastern edge of the northern Coast Ranges and western Sacramento Valley (e.g., *Prescott et al.*, 2001; *Trexler et al.*, 2022).

Seismic reflection data from Shell Oil seismic line 806, which were collected near Wilbur Springs, reveal a shallowly west-dipping reflector between approximately 6 and 10 km depth (*Constenius et al.*, 2000). The reflector coincides with microseismicity data, suggesting a possible reactivated tectonic wedge fault at depth below the Wilbur Springs area (*Wentworth et al.*, 1984; *Melosh and Langenheim*, 2022; *Langenheim et al.*, 2024). Southeast of Wilbur Springs, two large antiformal structures are located at the Rumsey and Dunnigan Hills (Figure 1). These structures are cored by active thrust and reverse faults (*Unruh et al.*, 1995) and have uplift rates of approximately 0.07 ± 0.01 mm/yr (*Cyr*, 2013).

2.3 Springs

The broader Geysers–Clear Lake region is renowned for its hot springs and geothermal resources (*McLaughlin*, 1981b). In a detailed sampling effort, *Thompson et al.* (1981) located, mapped, and sampled 113 hot springs, cold springs, and shallow wells and analyzed their fluid geochemistry. This database reveals several springs along the BSF including Crabtree Springs, Newman Spring, Bartlett Springs, Allen Springs, and Chalk Mountain Spring, among others (Figure 2). The springs along the Cross Springs Fault include Cross Spring, Hog Hollow Spring, and the Spring in Sweet Hollow Creek, among others. The Wilbur Springs area hosts the four hottest springs in the study area, including Wilbur Springs, Elgin Mine, Blank Spring, and Jones Fountain of Life Spring (Figure 3, Table 1). The position of springs along the BSF and Cross Springs Fault, and adjacent to structures in the Wilbur Springs area, suggests that spring locations are, at least in part, structurally controlled.

Table 1 – Temperatures of selected hot springs at or above 30 °C (*Thompson et al.*, 1981) and associated structures.

Hot spring name	Temperature (°C)	Structure
Jones Fountain of Life	61	Wilbur Springs antiform
Elgin Mine	54	Wilbur Springs antiform
Wilbur Springs	50	Wilbur Springs antiform
Blank Spring	44.5	Wilbur Springs antiform
Hog Hollow Spring	30	Cross Springs Fault
Newman Spring	43.5	Bartlett Springs Fault
Main Crabtree Spring	41	Bartlett Springs Fault
Upper Crabtree Spring	36	Bartlett Springs Fault

Detailed geologic mapping in the Wilbur Springs area (*McLaughlin et al.*, 1990) reveals significantly more springs and seeps than those sampled by *Thompson et al.* (1981) (Figure 3). This aligns with observations of geothermal geologists who report finding multiple unmapped or unknown springs within a given area during exploration (G. Melosh, oral

communication, 2025). Using silica, Na-K-Ca, and sulfate-isotope geothermometers, *Muffler* (1978) estimated fluid reservoir temperatures across the western United States, including a reservoir temperature of 144 ± 2 °C at Wilbur Springs (ws) and a temperature of 113 ± 5 °C at Chalk Mountain Spring (cms). The temperature estimate at Chalk Mountain Spring was based on silica geothermometry, and *Muffler* (1978) cautioned that it was likely not reliable due to low flow rates and high Mg and HCO_3 concentrations. At Wilbur Springs, temperature estimates were based on two reported downhole temperature measurements of 141 °C and a subjective estimate of 150 °C (*Muffler*, 1978).

3 Methods

3.1 Geothermometry

Geothermometry identifies chemically distinct zones of fluid circulation and estimates their source temperatures. This allows for a comparison of structural controls and serves as a proxy for depth of fluid circulation in different structural settings. To accomplish this, we use data from 30 springs, hot springs, and shallow wells located along or adjacent to the BSF, Cross Springs Fault, and in the Wilbur Springs area (Figure 2; *Thompson et al.*, 1981). Selected hot springs with temperatures of 30 °C or higher are summarized in Table 1.

To estimate fluid circulation temperatures, we input geochemical data into the *Powell and Cumming* (2010) geothermometer spreadsheet and used the Na-K-Mg geothermometer (*Giggenbach*, 1988) and the silica geothermometer (*Fournier and Potter*, 1982) plotted against $\log(K^2/Mg)$. These geothermometers were selected due to their widespread application and use in many geothermal studies (*Powell and Cumming*, 2010). We used two geothermometers to compare results and improve confidence in the interpretations.

The Na-K-Mg geothermometer is widely used to estimate fluid reservoir temperatures (e.g., *Romano and Liotta*, 2020). This geothermometer works on the premise that as hot fluids decrease in temperature the rate of water–rock interactions decreases rapidly as rock cations are unable to exchange with solution, effectively locking in a fluid Na-K ratio at a higher temperature than the Mg-K ratio (*Giggenbach*, 1984, 1986). Visual representation of these data in a ternary Na-Mg-K diagram allows for comparison of datasets and interpretation of partial equilibration temperatures (*Giggenbach*, 1988).

Silica geothermometry works on the premise that silica content in hot springs approximates circulation temperature due to the temperature dependence of silica solubility (e.g., *Verma*, 2000, and references therein). However, the *Fournier and Potter* (1982) geothermometer, which is used in *Powell and Cumming* (2010), tends to underestimate source fluid temperatures (e.g., *Verma*, 2000; *Nitschke et al.*, 2018) due to fluid mixing and the relatively rapid equilibration of silica concentration as the ascending fluid cools along its flow pathway.

Fluid circulation temperatures deduced by geothermometry are necessarily imprecise due to a range of unconstrained variables, including flow rates, fluid–rock interaction surface area, and mineral dissolution and precipitation rates, among others (e.g., *Giggenbach*, 1986; *Verma*, 2000). There may also be limitations to this method on the temporal scale related to flow rates or changes in flow rates with time. However, the current study requires only approximate or relative temperature estimates from different systems with distinct structural controls. A precise reservoir temperature is not imperative and small uncertainties in temperature will not affect interpretations.

3.2 Structure and Dilation Tendency

We performed a two-dimensional dilation tendency analysis to identify faults that are suitably oriented for dilation in the modern stress field. Dilation tendency (T_d) is the natural tendency of a fault or fracture to open due to its orientation in a given stress field. It is defined as:

$$T_d = (\sigma_1 - \sigma_n)/(\sigma_1 - \sigma_3) \quad (1)$$

where σ_1 and σ_3 are the maximum and minimum principal stresses and σ_n is the normal stress (*Ferrill et al.*, 1999, 2020). Faults with a high dilation tendency may be open, but the degree to which they provide fluid pathways will also depend on rock stiffness and local fault surface geometry and roughness as well as changes in differential stress with depth (e.g., *Sibson*, 1996).

Faults mapped by *McLaughlin et al.* (1990) and *Mclaughlin et al.* (2018), and Quaternary faults with a "good" certainty attribute (*U.S. Geological Survey*, 2004) were compiled into a GIS database. Spring locations (*Thompson et al.*, 1981) were plotted on the fault database map over one-meter-resolution lidar data (*U.S. Geological Survey*, 2018) to identify spatial correlations and potential structural controls on spring positions.

Faults were split into 10-meter intervals, creating a total of 78,846 fault segments. Some fault segments were shorter than 10 meters if the total fault length was not an exact multiple of 10 m. Fault strike was calculated for each fault segment in ArcGIS Pro and then used to calculate dilation tendency (*Melosh*, 2025). We assumed a fault dip of 90° because the majority of faults are strike-slip and exposure is poor so that measuring fault dip on most faults is not possible.

Consistent with the right-lateral strike-slip motion of the larger San Andreas Fault System, we assume a strike-slip stress regime, where the maximum principal stress is horizontal and the intermediate principal stress is vertical. The assumption of vertical fault planes means the normal vector (pole) to the fault has no vertical component and the resolved normal stress on the plane is controlled only by the horizontal stresses. Under these

conditions, σ_2 does not contribute to σ_n and our analysis becomes effectively two-dimensional.

We performed the two-dimensional dilation tendency analysis on each fault segment by applying total principal stress magnitudes of 50 MPa (σ_1) and 5 MPa (σ_3) (*Lozos et al.*, 2015), assigning S_{Hmax} as the maximum principal stress (50 MPa) and S_{hmin} as the minimum principal stress (5 MPa). The analysis uses a maximum horizontal stress (S_{Hmax}) orientation of N26°E (*Provost and Houston*, 2003).

We derived principal stress magnitudes from *Lozos et al.* (2015), who adjusted them in a BSF fault model until they produced an average stress drop of 9 MPa, consistent with microseismicity on the Hayward Fault. Stress drop on the Hayward Fault was used as a proxy because it is a nearby, semi-creeping fault in the northern San Andreas system, whereas the stress drop on the Bartlett Springs Fault is not well constrained (*Lozos et al.*, 2015). *Provost and Houston* (2003) determined the S_{Hmax} orientation in a stress inversion study, reporting an average orientation across the northern San Andreas Fault System (Figure 1). Stress inversions with fewer microseismic events or limited focal mechanism variability have greater error associated with them (*Provost and Houston*, 2003). We used reported error ranges on stress orientation data in a three-dimensional sensitivity analysis.

3.2.1 Three-Dimensional Sensitivity Analysis

To account for uncertainties introduced by the two-dimensional dilation tendency analysis, we performed a three-dimensional sensitivity analysis that incorporates plausible variations in fault geometry, principal-stress orientation, and depth-dependent stress magnitude. Whereas the two-dimensional analysis assumes vertical faults—such that the intermediate principal stress, σ_2, does not contribute to the resolved normal stress—the sensitivity analysis evaluates dipping faults under a full three-dimensional stress tensor.

We first evaluated sensitivity to stress orientation by repeating the analysis with S_{Hmax} oriented N20°E, the mean orientation from the six stress-inversion locations within the study area (Figure 1; *Provost and Houston*, 2003). We also varied the plunge of the maximum principal stress from 6° to 20°, consistent with the uncertainty reported by *Provost and Houston* (2003). For these orientation tests, we retained the stress magnitudes used in the primary analysis ($\sigma_1 = 50$ MPa and $\sigma_3 = 5$ MPa) and assigned $\sigma_2 = 20$ MPa (*Lozos et al.*, 2015).

We then evaluated the sensitivity of T_d to fault dip and depth-dependent stress conditions from the surface to 5 km depth under strike-slip, normal, and reverse faulting regimes. Fault dips ranged from 50° to 90° in the strike-slip and normal regimes and from 30° to 70° in the reverse regime. Vertical stress increased with depth according to lithostatic loading, assuming a rock density of 2,700 kg/m^3, while pore-fluid pressure followed a hydrostatic gradient. Horizontal stresses were calculated at each depth from the vertical stress and pore-fluid pressure using a friction coefficient of 0.6 and assumptions specific to each faulting regime. The principal stresses were ordered accordingly, with vertical stress corresponding to σ_2 in the strike-slip regime, σ_1 in the normal regime, and σ_3 in the reverse regime. For the normal and reverse regimes, σ_2 was assigned an intermediate value using a heuristically selected fraction of the interval between σ_1 and σ_3, placing it near the mean stress. Differential stress developed with depth from zero at the surface rather than being prescribed at a reference depth. These stress profiles were used to calculate T_d for northeast- and northwest-striking fault sets across the specified dip ranges, allowing comparison of the effects of fault geometry and stress regime under the assumed depth-dependent conditions.

Lastly, because the modeled fault orientations cannot capture the full geometric and kinematic variability of the natural fault system, we complement the dilation tendency and three-dimensional sensitivity analyses with detailed field observations where available. Measurements of fault geometry, slip indicators, deformation textures, and mineralization provide an independent framework for evaluating fault reactivation and rotation, local variations in the stress field, and the evolution of fluid pathways through time.

3.3 Thermal Drone Imagery

We collected predawn thermal small Unmanned Aircraft System (sUAS) imagery along two roughly orthogonal transects, the first trending NE and the second trending WNW, near Wilbur Hot Springs along Sulphur Creek, between 3:11 and 5:24 a.m. on 20 February 2025. The flights were repeated with a visible-light camera after sunrise. The flights covered approximately 0.23 and 0.30 km^2 (57 and 74 acres) for the NE and WNW transects, respectively. The axial parts of the surveyed areas have low relief, with increasing elevations along the edges of the valley floor. Ground cover included low grass, isolated trees, and water on the valley floor, and increasing scrub and forest cover on the valley walls. The areas also included exposed bedrock, historic mine workings, roads, and dwellings. The weather was cool and still, with high humidity and heavy frost formation by the end of the survey. Weather conditions the previous day were cool and windy with intermittent rain. For more details on flight parameters, see *Callahan and Hart-Wagoner* (2025).

Thermal flights were conducted with a DJI Mavic 3T with an Emlid RS2+ base station and Real-Time Kinematic (RTK) units. The base station was not located at a known point, nor did it have Long-Term Evolution (LTE) access to an RTK network for fixing locations, but the added GPS reference provides more stable and precise flight. Flight elevations were modified before constructing the models by correcting altitudes above launch pads based on elevations extracted from 3DEP lidar (*U.S. Geological Survey*, 2026). Ground control points were surveyed with a BadElf Flex Mini

Extreme, but, with no RTK connection via LTE, the error is greater than 1 m at most sites.

Thermal IR images were tuned for each flight using the DJI Thermal Analysis Tool and an ImageJ plugin (*Irujo*, 2022). Tuning parameters include distance, reflected (ambient) temperature, emissivity, and humidity. Calibration was conducted by iteratively processing time-stamped images that contained instrumented and surveyed temperature ground control points (TGCPs) and minimizing the difference between logged temperatures and the temperatures in tuned thermograms (*Melosh and Callahan*, 2026, data release). Images were batch-processed with the best-fit parameters and assembled into structure-from-motion models using Agisoft Metashape. Digital surface models (DSMs) as well as visible and thermal orthomosaics were exported for analysis in GIS software (*Melosh and Callahan*, 2026).

Both drone flight transects 1 and 2 (NE and WNW transects) were flown at 65-m altitude, producing DSMs and thermal mosaics with a resolution of about 9 cm/pixel. Data from both transects were combined. Visible-light DSMs and orthorectified photomosaics produced from 70-m altitude flights have a resolution of about 2 cm/pixel. Actual ground sampling distance changes across the maps based on altitude above uneven topography.

4 Results

4.1 Fault Observations

Fault exposures in Great Valley group sedimentary rocks occur along both the northeastern and southwestern sides of the Sulphur Creek valley. At 39.03456°N, 122.43440°W (black box in Figure 3), a fault surface oriented at 120/64 SW is exposed continuously for approximately 30 m (Figure 5a), striking within 10° of the Wilbur Springs antiform axis. Slickenlines on the fault surface are oriented at 225/62 SW, and multiple generations of overprinting slickenlines and slickenfibers are present (Figure 5b). Asymmetries in the quartz slickenfibers indicate reverse-sense motion, consistent with the kinematics inferred from Riedel shears. The principal fault surface lies within a deformation zone several meters wide that contains numerous vertical to subvertical subsidiary faults with steeply plunging slickenlines. Undeformed botryoidal silica locally coats the fault surface to thicknesses of several centimeters, and mosaic-textured, quartz-cemented breccia occurs within the surrounding deformation zone (Figure 5c).

Several additional, previously unmapped fault zones were identified between this exposure and the hydrothermal alteration zone north of Jones Fountain of Life Spring at 39.03473°N, 122.42887°W. Although less well exposed, these zones contain numerous small faults that strike predominantly northwest and range from shallowly dipping to subvertical. Slickenlines are common on these surfaces, but no kinematic indicators were identified. On the southwestern side of the valley, immediately south of the fault in Figure 5, at 39.03311°N, 122.43246°W, we mapped another fault oriented at 110/45 S; slickenlines on this fault surface have a trend and plunge of 216/43 SW. Numerous additional low-angle faults are exposed nearby but were not measured.

4.2 Geothermometry

Results from the Na-K-Mg geothermometer show partial equilibration temperatures ranging from 180 to 193 °C at Jones Fountain of Life Spring (jfl), Wilbur Springs (ws), Blank Spring (bs), and Elgin Mine (em) (Figure 6a, Table 2). All of these hot springs are located within <1 km of the hinge of the Wilbur Springs antiform (Figures 2, 3). Highway 20 Sulfur Spring (h20ss), located ∼6 km east of the Wilbur Springs antiform, has a partial equilibration temperature of 135 °C (Figure 6a). The remaining springs along the BSF, including Crabtree Springs (mc, uc), Newman Spring (ns), and Bartlett Springs (mb, ub), as well as springs along or near the Cross Springs Fault [Hog Hollow Spring (hh) and Quigley Soda Spring (qs)] plot within the immature water field (Figure 6a) and cannot be used to estimate deeper fluid circulation temperatures.

Temperatures derived from the silica geothermometer are consistent with Na-K-Mg results (Table 2). The four hottest hot springs in the Wilbur Springs area plot along or above the quartz solubility line between temperatures of 140–180 °C (Figure 6b). Highway 20 Sulfur Spring (h20ss) plots above the quartz solubility line at ∼110 °C (Figure 6b). Springs along or near the Cross Springs Fault including Quigley Soda Spring (qs), the Spring in Sweet Hollow Creek (shc), and Hog Hollow Spring (hh), plot at 110 °C, 80 °C, and 60 °C, respectively, between the chalcedony and β-cristobalite solubility lines (Figure 6b). Springs along the BSF also plot at lower temperatures. Chalk Mountain Spring (cms) plots at ∼90 °C above the α-cristobalite solubility line and Newman Spring (ns) and Crabtree Springs (mc, uc) plot along the β-cristobalite solubility line at a temperature of 60 °C (Figure 6b). Remaining springs plot below the 60 °C line.

4.3 Fault Geometry and Dilation Tendency

Dilation tendency analysis results display spatial correlations between fault segments with high dilation tendency and springs along the BSF, the Cross Springs Fault, and in the Wilbur Springs area (Figure 7). At Wilbur Springs, northeast-striking faults cross the regional structural grain and intersect northwest-striking faults at angles between ∼80° and 100°. On average, the northeast-striking faults strike at 35° ± 1°, have high dilation tendency values of 0.9 (Figure 8a), and range between 0.1 km and 2.5 km in length. Northwest-striking faults have low dilation tendency values of 0.1 (Figure 8a), and an average strike of 319° ± 2°, and reach up to 5.5 km in length.

The LIVFZ branches from the BSF and continues east toward Wilbur Springs for ∼11.5 km (Figure 2),

Table 2 – Geochemical data of springs, hot springs, and wells analyzed by *Thompson et al.* (1981) used in this study. Springs with an asterisk (*) symbol have updated latitude and longitude positions where visited in the field. All units are in mg/L, temperature in °C, and flow rate in L/min. Columns labeled NKM and KMS are the results from the Na-K-Mg and silica geothermometers, respectively, in units of °C. Column NKM omits springs that did not plot within partial equilibration. Column KMS omits temperature estimates <80 °C.

Spring Name	Label	Latitude	Longitude	Flow Rate	Temp.	pH	Li	Na	K	Ca	Mg	SiO_2	B	Cl	F	SO_4	HCO_3	NKM	KMS
Main Crabtree	mc	39.29167	122.82333	8	41	7.8	4.08	1850	36.5	51	198	158	277	1240	0.34	1	3850		
Upper Crabtree	uc	39.29	122.82167	0	36	6.1	0.015	18	5.2	70	43	52	0.1	9.8	0.34	285	104		
Rice Fork Eel River	rf	39.28833	122.81833	100	25	7.97	<0.01	10	1.4	32	9.8	27	0.33	9.1	2.3	8	164		
Newman Spring	ns	39.19833	122.71667	18	34.5	7.5	20	2500	56.5	162	520	134	386	3310	0.18	2	4290		
Royal Spring	rs	39.23	122.745	8	18	7.8	0.23	332	5.6	58	430	94	28	300	0.18	3	2780		
Main Bartlett	mb	39.185	122.70167	8	18.5	7.48	0.02	14	1.4	89	470		<0.1	8.4	0.39	9	2750		
Upper Bartlett	ub	39.18333	122.7	6	16	7.36	0.02	12	1.4	70	410	94	<0.1	8.4	0.32	1	2420		
Gas Spring	gs	39.18833	122.68833	0.8	12	6.61	0.01	17	1	65	32	34	0	4	0	120	167		
Allen Springs	as	39.16	122.665	20	18	7.61	2.37	292	8.6	130	360	100	41	481	<0.1	12	2000		
Hough Spring	hs	39.16167	122.61333	1	16	7.37	0.6	98	7.3	385	43	75	0.27	5	0.9	3	831		
Salt Lick Spring	sls	39.1	122.60667	24	22	7.96	0.67	367	12.3	108	390	100	48	419	0.16	4	2280		
Chalk Mountain Spring	cms	39.08	122.58333	0.4	24	7.58	5.2	1600	196	66	495	91	190	2410	0	32	3300		91
Cache Creek Magnesite spring	ccms	39.07333	122.56667	20	22	7.52	3.1	950	47	183	735	89	130	1920	0	265	2890		
Quigley Soda Spring	qs	39.05333	122.59667	4	28	7.72	4.8	1040	162	148	92	89	122	918	0	1	2260		109
Unnamed Cold Spring	ucs	39.05333	122.58833		19	7.84	<0.01	15	4	16.4	11.2	60	<0.01	22	0	1	88		
Cross Spring	x	39.04167	122.59		18	7.71	0.02	17	4	17	12.1	60	0	13	0	1	190		
Hog Hollow Spring	hh	39.02333	122.58833	40	30	7.26	0.48	200	15.2	106	46	136	14.5	174	0.33	4	862		
Spring in Sweet Hollow Creek	shc	39.01833	122.58333		22	7.47	1.8	580	48	155	78	96	49	561	0	175	1170		80
Well Benmore Canyon	wbc	39.025	122.57		21	7.75	3.4	2860	54	100	360	28	72	4050	1	400	3050		
Sulfur Spring	ss	39.09667	122.52333		20	8.07	0.28	322	9.2	23	12.9	146	18	331	0.89	26	72		
Grizzly Spring	gr	39.00167	122.49833		20	7.84	0.7	465	12	10	132	101	325	310	0	21	1225		
Highway 20 Sulfur Spring	h20ss	39.01667	122.49		23	7.57	0.53	1550	34	3.5	5	24	42	2080	7	7	498	135	106
Eagle Rock Spring	ers	39.06833	122.44		15.5	8.54	0.78	222	18	3.1	172	78	11	262	0	1	1100		
Jones' Fountain of Life Spring *	jfl	39.03333	122.445		61	8.75	8.4	10000	490	2.3	30	84	271	11900	3	80	4100	181	164
Wilbur Springs *	ws	39.04667	122.42167	80	50	8	8	9200	445	2.5	44	131	280	9810	2	390	7040	180	153
Turkey Run Mine	trm	39.01667	122.44		22	7.62	1.68	1064	35	21	770	70	35	1150	5	2400	2300		
Blank Spring *	bs	39.02333	122.43333		44.5	8.39	6.48	7600	409	2.2	70	113	158	8050	2	215	6800	187	142
Toby's Cold Well	tcw	39.035	122.42667		24.5	8.46	0.28	200	7	25	162	23	5	140	0	170	972		
Hayfield Well	hw	39.01833	122.40333		14.5	8.47	0.04	65	2	42	210	19	1	29	0	200	1060		
Elgin Mine	em	39.05833	122.475	20	54	7.93	12.5	9950	580	3.6	26	152	220	12100	3	105	7300	193	173

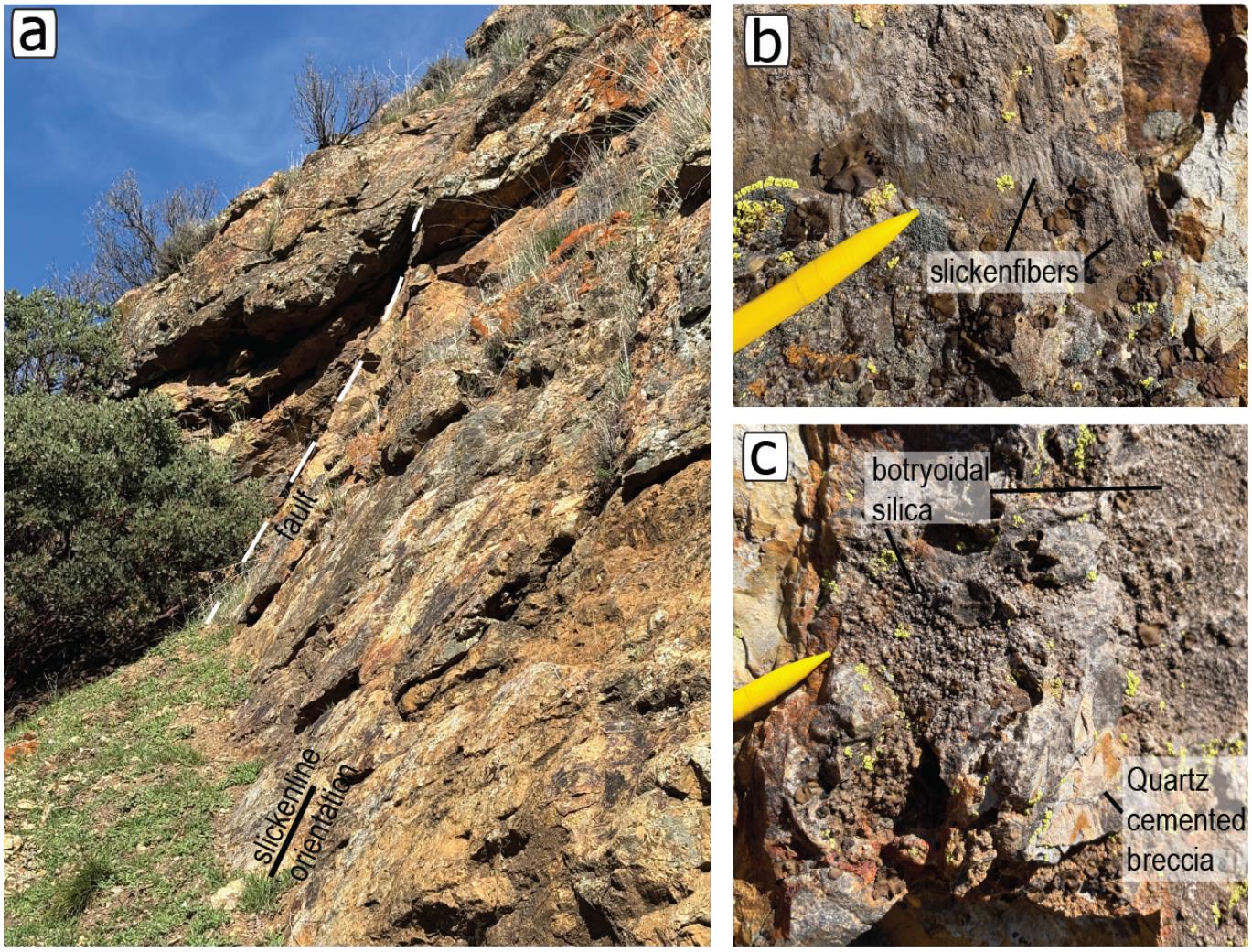

Figure 5 – Field photographs of a fault exposure on the northeast side of Sulphur Creek (39.03456°N, 122.43440°W; see Figure 3 for location). a) Fault surface with slickenline orientation marked by solid black line. b) Quartz slickenfibers on fault surface. c) Botryoidal silica and quartz-cemented breccia on fault surface. Photographs by Ben Melosh, U.S. Geological Survey, 2025.

at a strike of ∼110°, with correspondingly low dilation tendency values of 0.1 (Figure 7a). Elgin Mine is located within the easternmost extent of this fault zone, near the hinge of the Wilbur Springs antiform (Figure 7a).

The curvilinear Cross Springs Fault has dilation tendency ranging from 0.2 to 1.0, with a mean of 0.8 (Figure 7b) and higher values along the southern part of the fault. High dilation tendency values on or near the Cross Springs Fault coincide with five springs, including Hog Hollow Spring (hh) which has a temperature of 30 °C (Figure 7b). Cross Spring (x) is located directly on the surface trace of the Cross Springs Fault; Quigley Soda Spring (qs) and an unnamed cold spring (ucs) are located on an intersecting fault trace with low dilation tendency values.

Within the study area, the BSF has a strike of ∼311° NW, and a mean dilation tendency of 0.2 (Figure 8b). Although numerous springs are located along the BSF (Figure 2), spatial relationships between dilation tendency and springs are not obvious everywhere (Figure 7c, d). Additionally, except for Newman Spring and Crabtree Springs, these springs are primarily of lower temperature. Main and Upper Crabtree Hot Springs (mc, uc) are located on the mapped trace of the BSF with dilation tendency of 0.4 and no obvious structural irregularities observed at the scale of this study (Figure 7c). Newman Spring (ns) is located in contact with a serpentinite lens on an east–west-oriented fault trace with dilation tendency values between 0.3 and 0.8 (Figure 7d). Allen Springs (as) is located near the intersection of two fault traces with highly variable dilation tendency values between 0.1 and 0.9 (Figure 7d). Fault traces in the vicinity of Allen Springs (as) and Main and Upper Bartlett Springs (mb, ub) have a mean dilation tendency of 0.2 (Figure 7d).

4.3.1 Sensitivity Results

In this study, all faults are modeled as vertical planes and both σ_1 and σ_3 are horizontal; fault-plane normals lie within the horizontal σ_1–σ_3 plane. Under this simplified geometry, σ_2 does not contribute to the resolved normal stress, and T_d reduces to a function of orientation alone. Therefore, variations in stress magnitude or stress ratio do not affect calculated T_d

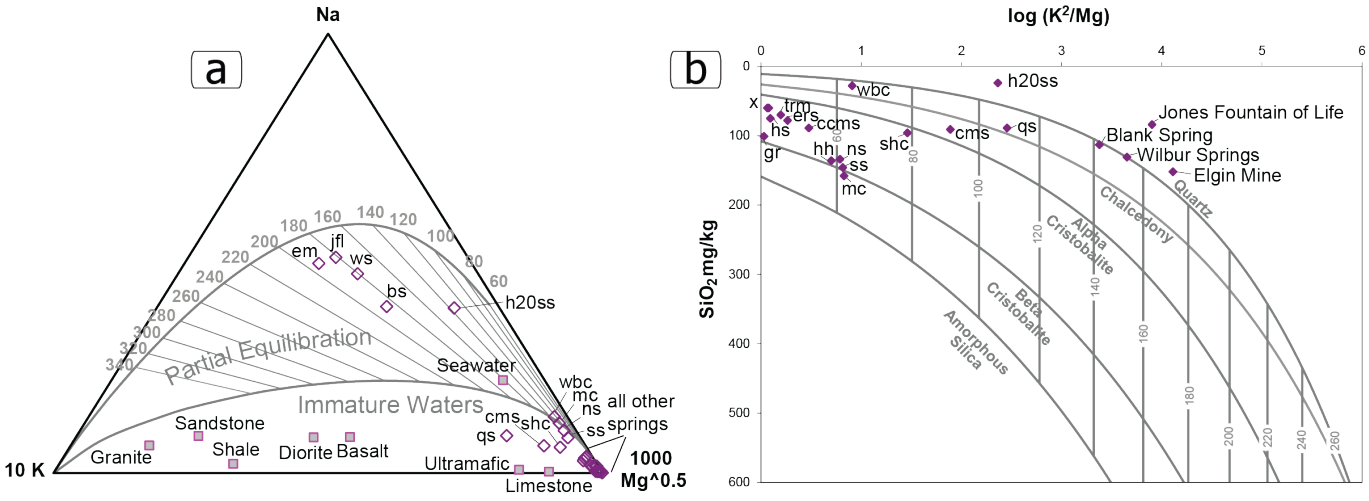

Figure 6 – Fluid geochemistry and geothermometry results. a) Giggenbach plot (*Giggenbach*, 1988) showing partial equilibration temperatures of 180–190 °C for hot springs in the Wilbur Springs area, jfl: Jones Fountain of Life Spring, em: Elgin Mine, ws: Wilbur Springs, and bs: Blank Spring. Spring name abbreviations match those listed in the text and map (Figure 2), and include h20ss: Highway 20 Sulfur Spring, wbc: Well in Benmore Canyon, mc: Main Crabtree Spring, ns: Newman Spring, ss: Sulfur Spring, qs: Quigley Soda Spring, cms: Chalk Mountain Spring, shc: Spring in Sweet Hollow Creek. b) Silica geothermometry results, hot springs in the Wilbur Springs area record source fluid temperatures from the silica geothermometer of 140–180 °C along the quartz solubility line. Additional spring name abbreviations are hh: Hog Hollow Spring, ccms: Cache Creek Magnesite Spring, ers: Eagle Rock Spring, trm: Turkey Run Mine, x: Cross Spring, gr: Grizzly Spring, hs: Hough Spring. Springs with geothermometry below 40 °C are omitted.

values unless fault dip or principal stress orientations are varied. In reality, fault networks and the stress field are inherently three-dimensional, and we approximate this complexity by incorporating uncertainties in stress orientation and magnitude across a range of assumed fault dips (Figure 9).

Recalculating the dilation tendency analysis with an average S_{Hmax} of N20°E (Figure 1) resulted in a minor, yet statistically significant, decrease in dilation tendency across all fault segments of 0.04 on average, with a maximum decrease and maximum increase of 0.10, or ∼10% of the original model. This adjustment would shift the optimal strike of statically open faults by 6° to the north.

Varying the three-dimensional orientation of the stress field relative to the dip of different faults to account for angular uncertainty of the stress inversions changes dilation tendency (Figure 9a). Performing the T_d analysis with a shallowly plunging σ_1 of 6° results in an average T_d difference of 0.005, whereas a plunging σ_1 of 20° results in an average T_d difference of 0.05 over the entire study area. These are very small differences. However, in the Wilbur Springs area, varying the plunge of σ_1 by a maximum of 20° results in differences of dilation tendency results on the order of ±0.2 for faults dipping between vertical and 50° (Figure 9a). Adjusting the trend of σ_1 by ±20° results in changes to T_d as high as 0.4.

To test the sensitivity of the model to fault dip, we recalculated dilation tendency over a range of possible fault dips for the northeast- and northwest-striking fault populations in the Wilbur Springs area (Figure 9). In a strike-slip setting, dilation tendency of non-vertical faults is sensitive to changes in differential stress with depth, and more gently dipping faults display a greater sensitivity (Figure 9b). Dilation tendency on northeast-striking faults with 50° dips is reduced by ∼0.3 at low differential stress near the surface, and is reduced by ∼0.2 at higher differential stress at depths of 5 km (Figure 9b). Northwest-striking faults show almost no change in dilation tendency at low differential stress, and an increase of ∼0.1 at higher differential stress at 5 km (Figure 9b). Normal and reverse faulting regimes also display a depth-dependence of dilation tendency for steeply to moderately dipping faults. Normal faulting regimes have overall higher dilation tendency for both fault populations when compared to strike-slip or reverse faulting regimes (Figure 9b).

This sensitivity analysis uses a single depth-dependent stress profile for each faulting regime rather than a range of plausible stress gradients within each regime. The plotted T_d ranges therefore do not represent the full uncertainty associated with the assumed stress profiles. Nevertheless, the analysis provides a first-order assessment of how T_d varies with fault dip and faulting regime under the prescribed stress conditions.

4.4 Thermal Drone Imagery

Thermal drone imagery reveals a preferred northeast alignment of hot springs and seeps along Sulphur Creek, including several previously unidentified point sources (Figure 10). This orientation matches many of the northeast-striking faults in the Wilbur Springs area. Background water temperature conditions (10.4

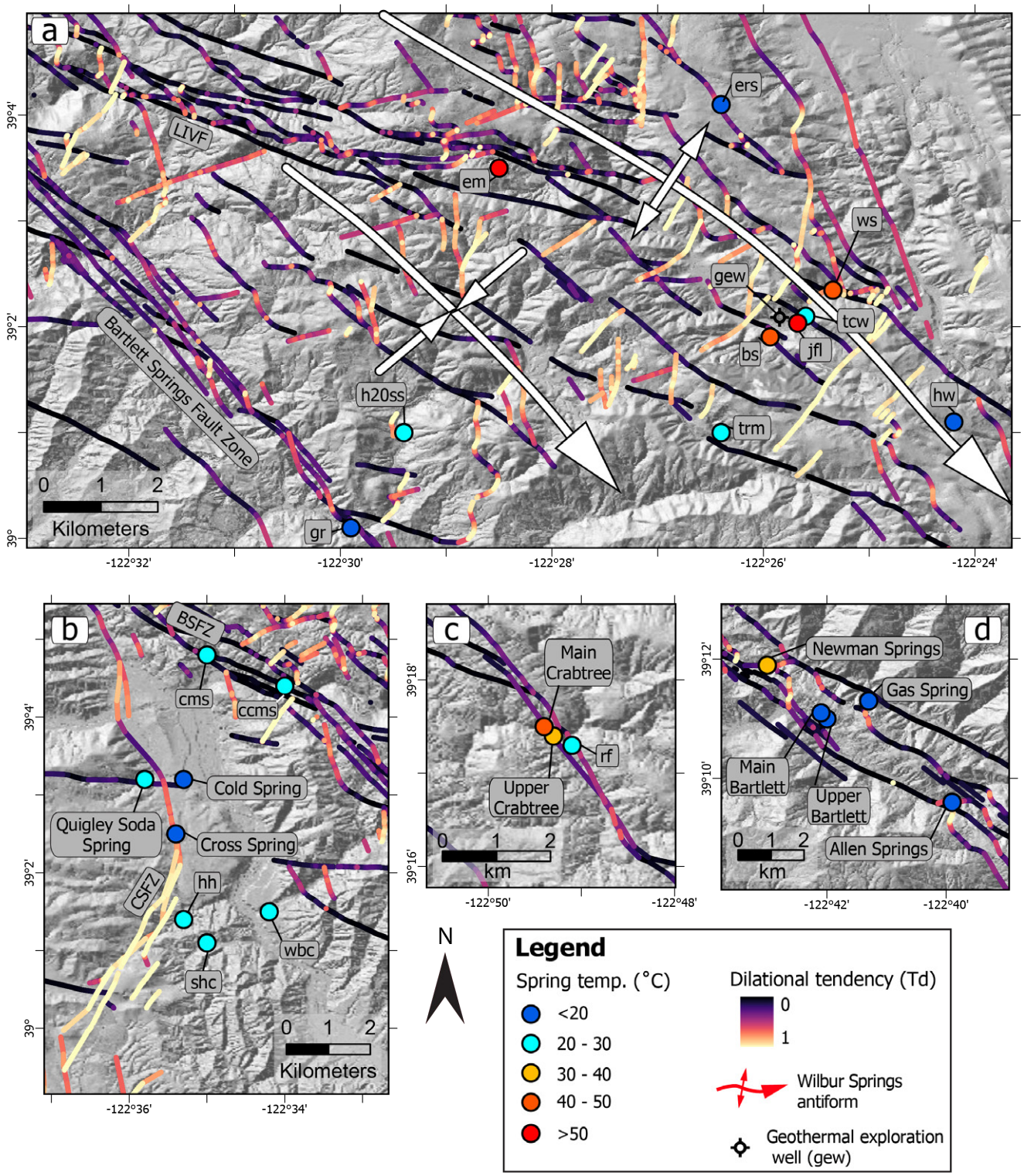

Figure 7 – Dilation tendency results mapped onto faults with spring locations (*Thompson et al.*, 1981) and the position of the Wilbur Springs antiform (*Mclaughlin et al.*, 2018), displayed on one-meter-resolution lidar data (*U.S. Geological Survey*, 2018). Boxes a–d in Figure 2 correspond to panels a–d of this figure. a) The Wilbur Springs area (also shown in Figure 3), b) Cross Springs Fault, c) Bartlett Springs Fault at Crabtree Hot Springs, d) Bartlett Springs Fault at Bartlett Springs.

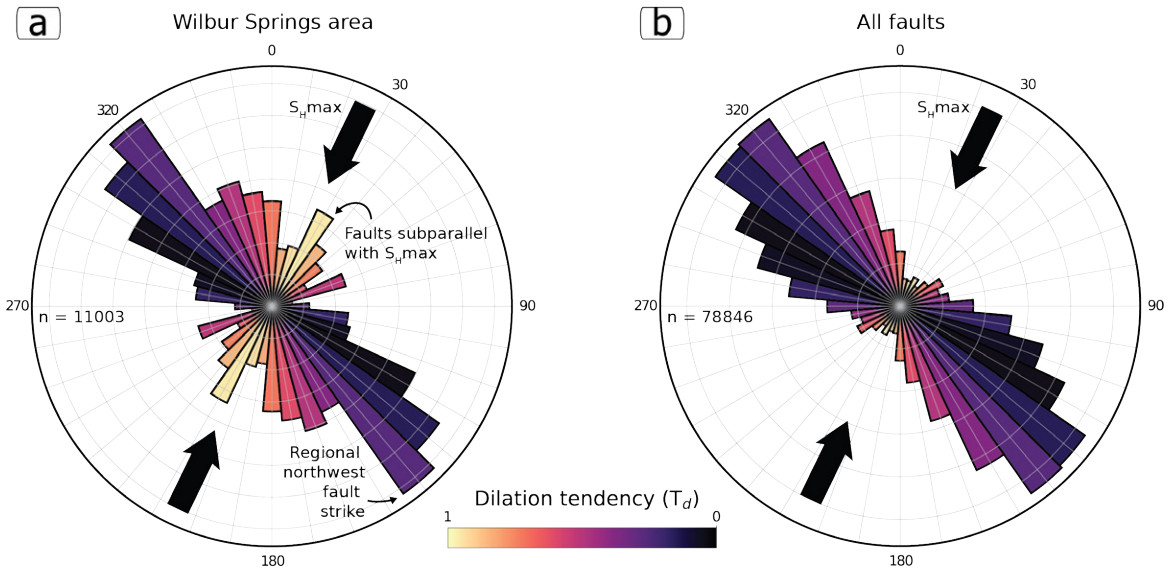

Figure 8 – Rose diagrams of fault orientation and dilation tendency. S_{Hmax}: Maximum horizontal stress. a) Faults within the Wilbur Springs area between, but not including, the BSF and the Little Indian Valley Fault Zone (LIVFZ). b) All fault segments included in the static stress analysis.

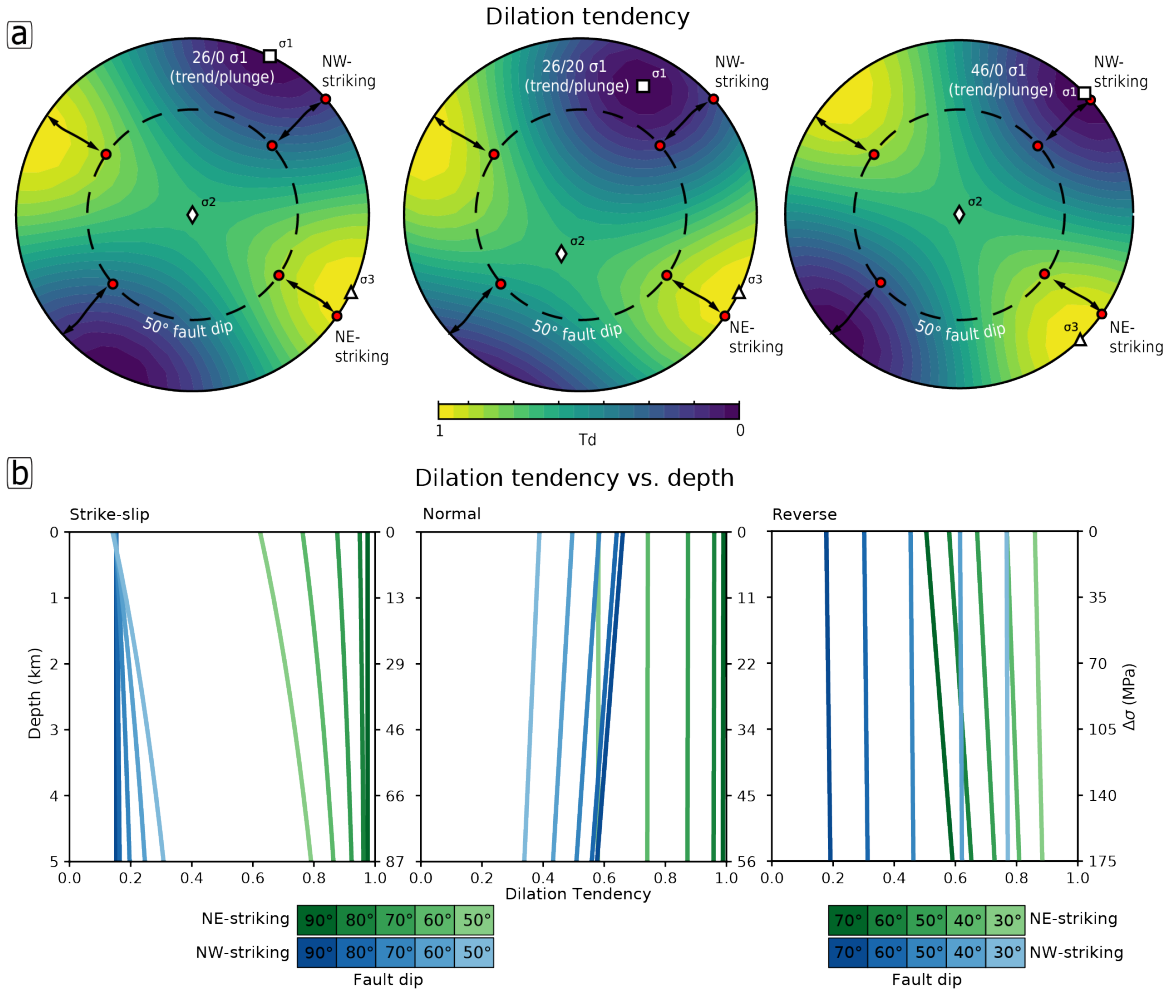

Figure 9 – Dilation tendency sensitivity to stress magnitude, orientation, and fault dip. a) Three stereonets showing the poles to the mean orientations (red circles) of northeast-striking and northwest-striking fault populations in the Wilbur Springs area; black arrows represent fault dip ranges between 90° and 50°. The black dashed small circle marks the 50° plunge of poles to faults of any strike. The first stereonet shows the stress orientation used in the dilation tendency analysis of this study, the second shows σ_1 plunging 20°, the third shows σ_1 rotated 20° to the east. b) The variation of dilation tendency with respect to differential stress for the mean strikes of northeast- and northwest-oriented faults in the Wilbur Springs area. Strike-slip, normal, and reverse faulting regimes are included for comparison. The range of dilation tendency values for 50°- and 90°-dipping faults is shown for each faulting regime.

± 0.3 °C; $n > 20{,}000$) were identified by extracting the calibrated water temperature in Sulphur Creek along a roughly 1.5-km-long channel profile upstream from hot spring influence. We identified points in the creek and valley with calibrated temperatures above 13.5 °C as anomalous, and recorded the highest single-pixel temperature anomalies within a radius of 35 m. All reported temperatures were calibrated in our study.

Using this approach, six anomalies occur in or along transect 2 (the WNW transect), mostly upstream from Jones Fountain of Life Spring, ranging in temperature from 14 to 19 °C. These are small point sources flowing from riverbanks or channels, plus one hand-dug well lined with stone walls to the SE that was previously identified as a spring but was not flowing. Eleven anomalies occur along transect 1 (the NE transect), ranging in temperature from 17 to 50 °C. These manifestations include Blank Spring and Jones Fountain of Life Spring, plus nine other warm seeps in or near the riverbanks. One small anomaly (16 °C) occurs near the intersection of transects 1 and 2, and another (15 °C) flows downslope from a warmer source off the map to the north (Figure 10). The identified anomalies generally correspond to mapped springs (Blank Spring, Jones Fountain of Life Spring). However, the temperatures are generally lower than reported and the locations of the reported springs are off by 30 m or more. Several surface anomalies near Jones Fountain of Life Spring ranging in temperature from 28 to 50 °C are not specifically identified in prior reports. None of the small anomalies in transect 2 (the WNW transect) were previously described.

The meadow at the intersection of the two flight transects (NE and WNW transects) appears colder than most surrounding areas, other than very-low-emissivity surfaces. The reason for this appearance is not known, but if real, could include changes in substrate due to past mining activity, increased evaporative cooling, or a combination of both.

The best-fit tuning parameters were D = 25 m, H = 96%, E = 0.95–0.96, and an ambient temperature of −2.6 °C. The tuned ambient temperature is usually lower than the recorded temperature (by ∼0.6–0.8 °C) to compensate for the actual flight altitudes. The average difference between measured temperature and calculated model temperatures in the thermal mosaic at TGCPs is 0.0 °C; the largest difference is −0.8 °C. The difference between measured temperatures at one check point not used in calibration (an instrumented shallow puddle) was −0.9 to −2.1 °C. An additional check point was instrumented but not used because the water level dropped substantially overnight.

5 Discussion

Here we present interpretations while acknowledging the limitations and uncertainties arising from the range of variables that influence the results. We also evaluate how these uncertainties affect the robustness of our conclusions and identify where additional constraints are needed.

In this study, we use the term fluid circulation to encompass the downward migration of meteoric fluids, the upward flow of heated waters, and movement of fluids at depth. We did not map pathways of downwelling fluids, yet it is reasonable to assume they occur separately from upwelling zones, because direct overlap would cool the ascending thermal waters.

5.1 A Conceptual Model for Fluid Circulation in Transpression

The geothermometry results reveal a distinct contrast across the study area: the BSF is the dominant regional structure, but it primarily hosts low-temperature circulation; the Wilbur Springs area, which lacks a major through-going fault, records the highest fluid temperatures. To explain this, we propose an integrated conceptual model where fluid circulation in an active transpressional zone is facilitated not by the primary plate-boundary-scale structure, but by the spatial overlap of three secondary fluid-pathway-generating mechanisms.

In this framework, for much of its length, the BSF acts as a statically closed fluid barrier under the modern stress field, effectively inhibiting deep-seated circulation. High-temperature upwelling is instead focused away from the BSF into the adjacent Wilbur Springs antiform, where the convergence of (1) localized tensile stress in the active fold hinge, (2) secondary faults optimally oriented for dilation, and (3) plunging fault intersections creates a robust permeability network (Figure 11). This multi-factor model accounts for the presence of hydrothermal systems reaching ∼190 °C within a contractional regime by identifying how these specific structural elements culminate in potential fluid pathways that extend to depths of several kilometers.

5.1.1 The Role of the Antiform

The presence of the large, active antiform introduces tensile stress focused along the structurally higher part of the fold hinge (Figure 11). Ongoing deformation and local uplift are suggested by the presence of elevated fluvial terraces near the fold hinge, similar to actively uplifting structures like the Rumsey and Dunnigan Hills to the southeast (*Cyr*, 2013). These active hinges provide a localized mechanical environment conducive to the maintenance of open fractures. This is supported by the spatial proximity (<1 km) of the highest-temperature manifestations, such as Wilbur Springs, Jones Fountain of Life Spring, and Elgin Mine, to the axial trace of the Wilbur Springs antiform (Figure 7a).

Stress and strain vary systematically with depth across folds, producing contrasting effects on subsurface fluid flow. Beneath the antiform, contraction at depth combined with dilation and extensional strain at shallower levels would enhance upward flow by generating pressure gradients that drive fluids toward

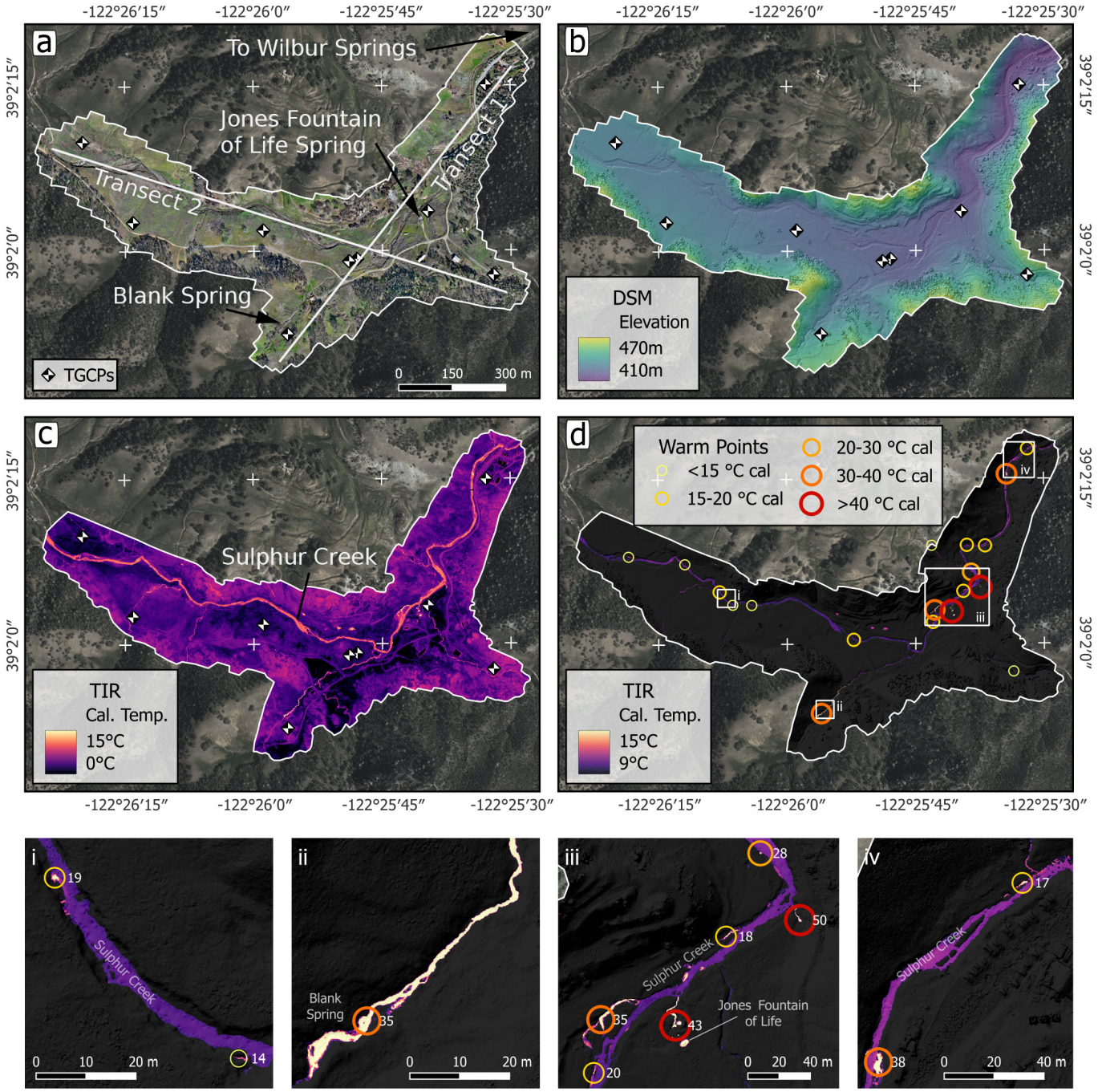

Figure 10 – Processed sUAS products from Sulphur Creek near Wilbur Hot Springs, including a) visible-light orthomosaics, b) topography (digital surface model) from visible-light models, c) calibrated thermal mosaic, and d) thermal mosaic clipped to calibrated temperatures >9 °C showing discrete temperature anomalies measured as the warmest points within a 35-m radius. Insets i–iv show small, lower-temperature seeps in the upstream reach of Sulphur Creek (WNW-oriented transect 2) and larger, warmer seeps and springs in the NE-oriented reach (transect 1). Data available at *Melosh and Callahan* (2026).

the surface. In contrast, beneath the synform, the opposite configuration would be expected, with dilation concentrated at depth and contraction above, creating a reversed hydraulic gradient that prevents upwelling (Figure 11). At Highway 20 Sulfur Spring, this may generate conditions for a blind hydrothermal system; however, because the BSF is located less than 2 km west, a potential role of the fault as a structural control cannot be ruled out.

5.1.2 Stress Rotation at the Fold Hinge

Tensile stresses that develop in fold hinges represent local departures from the uniform regional stress field assumed in our analysis. In the upper hinge of the Wilbur Springs antiform, the tensile stress may be oriented nearly opposite to the regional orientation of S_{Hmax}. Consequently, faults with high T_d under the regional stress field may have low T_d near the fold hinge, a local effect not captured by our T_d maps. Moreover, as the fold grew and the local stress field evolved, different fracture sets may have become favorable for fluid flow

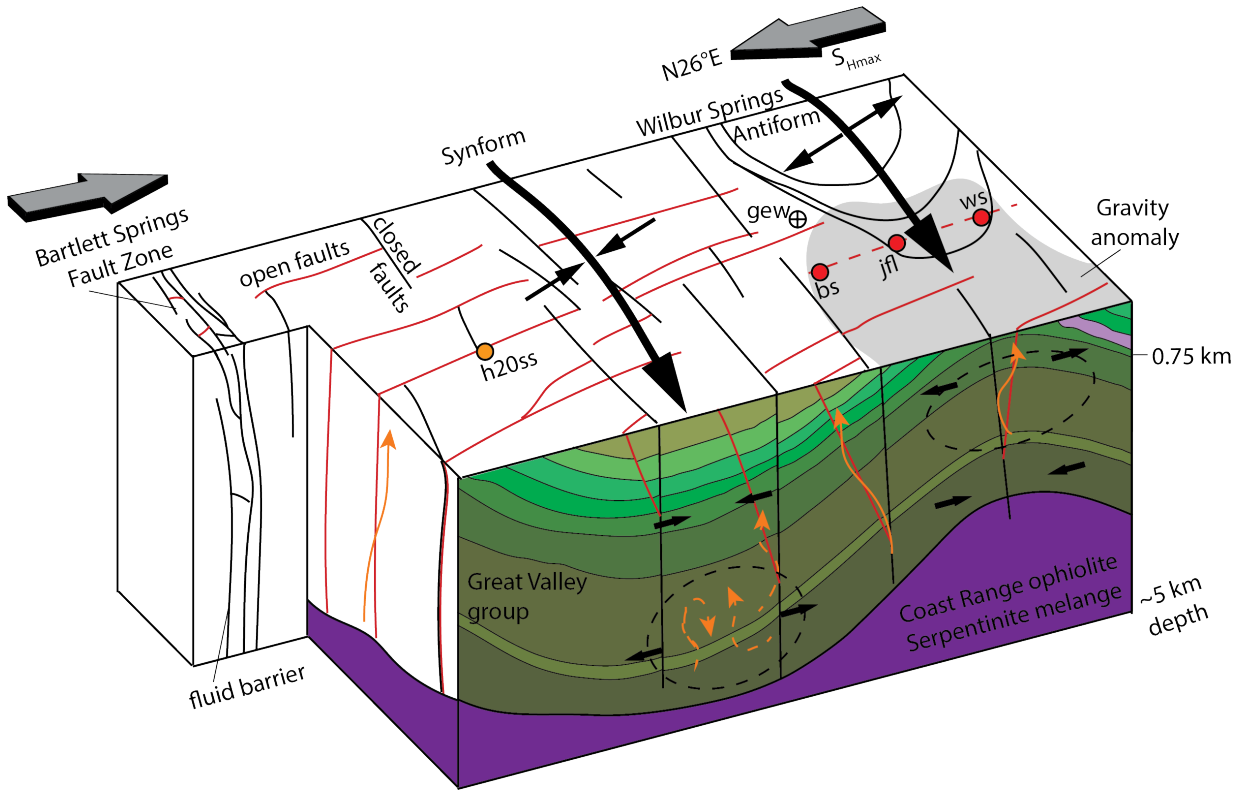

Figure 11 – Schematic three-dimensional block diagram illustrating the conceptual structural model. Faults at a high angle to the BSF are subparallel to the maximum horizontal stress. In combination with tensile stress in fold hinges, this may promote fluid circulation and migration from depth along steeply plunging fault intersections. Black dashed ovals represent theoretical areas of increased tensile stress in fold hinges as depicted with small black arrows. Orange arrows and dashed arrows represent fluid circulation. Spring name abbreviations match those listed in the text: ws: Wilbur Springs, jfl: Jones Fountain of Life Spring, bs: Blank Spring, h20ss: Highway 20 Sulfur Spring. gew: geothermal exploration well.

at different times. Fold-limb rotation may also have reoriented existing faults, while continued deformation generated new fractures. Although these processes are not incorporated into our numerical analysis, field evidence from the Wilbur Springs area records multiple episodes of fault slip, reactivation, fluid flow, and mineral precipitation.

This history is particularly well expressed by the fault described in Section 4.1 and shown in Figure 5. We interpret this structure as a reverse or thrust fault, similar to the nearby low-angle faults exposed south of the Sulphur Creek valley, that was subsequently rotated together with the surrounding bedding. As the Wilbur Springs antiform began to form, rotation of the local stress field near the antiform hinge reoriented σ_3 approximately normal to the strike of the fault. Under these conditions, the fault could have been reactivated as a normal fault, creating additional space for fluid flow and contributing to the development of the Wilbur Springs hydrothermal system.

Fault reactivation is supported by multiple overprinting generations of slickenlines and slickenfibers (Figure 5) indicating changes in slip direction. The presence of both quartz slickenfibers and undeformed botryoidal silica indicates that quartz precipitation occurred both syn- and post-kinematically. The fault therefore likely served as a fluid conduit for an extended period of time. Quartz-cemented mosaic breccia provides further evidence for fluid flow and mineral precipitation within dilatant fault-hosted zones.

Although most of the observed kinematic indicators on this fault imply reverse-sense motion in its present orientation, this interpretation assumes that the fault has not been overturned since slip occurred. If the fault is overturned, the same kinematic indicators would instead record normal-sense motion. However, this cannot be determined with the present data, so we only recognize it as an alternative possibility. Regardless of the sense of motion, the presence of hydrothermal quartz indicates it was a fluid pathway for the Wilbur Springs hydrothermal system.

While rotation of the local stress field within the fold hinge would make northeast-striking faults less favorable for dilation, it would have the opposite effect on northwest-striking faults, including the fault described above (Figure 5). Moreover, a hinge-related stress rotation would affect only portions of the northeast-striking faults as their full lengths extend well past the hinge zone. Thus, although our conceptual model identifies three mechanisms that collectively promote fluid flow, it necessarily simplifies a system in which fault growth and reactivation, spatial and depth-dependent variations in stress orientation, and the rotation of fault and fracture sets may produce substantial local variability in fluid-flow potential.

5.1.3 Fault Orientations and Intersections

While the regional S_{Hmax} orientation (N26°E) imposes transpressional strain on the BSF ($T_d = 0.2$), northeast-striking faults are comparatively well oriented for dilation under the regional stress field ($T_d = 0.9$), and may therefore form important fluid-flow pathways where that stress orientation is locally maintained. Their potential to transmit fluid may be reduced where the stress field rotates within the Wilbur Springs antiform hinge. Nevertheless, the northeast alignment of springs and seeps suggests that northeast-striking structures exert a first-order control on fluid flow across the broader Wilbur Springs area (Figures 7, 10). This relationship emphasizes that T_d describes the relative favorability of a fault orientation for dilation under an assumed stress state, rather than its absolute capacity to transmit fluid, which also depends on local stress variations, connectivity, inherited fault-zone architecture, and fracture-scale mechanical properties.

Fluid upwelling may be further enhanced where northeast-striking faults intersect northwest-striking faults. These intersections plunge moderately to steeply to depth, forming vertically oriented pathways that may connect shallow circulation systems to deeper fluid sources. Such fault intersections provide geometrically favorable conduits for focused fluid ascent, consistent with observations from other tectonic settings where intersecting fault networks localize permeability and fluid flow (*Faulds and Hinz*, 2014).

5.2 Conditions for Fluid Circulation

5.2.1 The Bartlett Springs Fault

For much of its length, the BSF is statically closed under the modern stress field, inhibiting fluid circulation (Figures 8b, 11), except for localized releasing step-overs or fault bends (Figure 7b–d). Although warm springs are present along the BSF, fluid mixing with meteoric water appears to be pervasive, as indicated by elevated Mg values. Geothermometry results primarily suggest low-temperature water–rock interactions occurring near the surface (Figure 6; *Nicholson*, 1993).

Many of the warm springs on the BSF lack obvious spatial correlation to dilational irregularities or high-T_d values (Figure 2). For example, Crabtree Hot Springs (Figure 7c) does not show a clear association with high dilation tendency fault segments. This discrepancy may, in part, result from the scale and two-dimensional nature of this study, which does not account for subsurface fault geometry or roughness that could influence spring locations. For instance, Main and Upper Bartlett Springs are located between two mapped strands of the BSF, which dip steeply to the east (*Mclaughlin et al.*, 2018). At a more localized scale, fault zone structures are more complex than depicted in this fault model, potentially resulting in the omission of important structural features. Additionally, local stress variations not captured in our analysis could amplify the importance of even small changes in fault orientation.

The lack of correlation between warm springs and high dilation tendency on the BSF reflects the influence of additional factors that control fluid flow as discussed in Section 5.2.4. Although favorably oriented faults can facilitate deep fluid circulation, T_d does not everywhere predict it.

5.2.2 The Cross Springs Fault

High dilation tendency (Figure 7b) and spring clusters along and near the Cross Springs Fault suggest it maintains open fluid conduits. However, spring temperatures are relatively low (<60 °C) and inferred source fluid temperatures from geothermometry are low, except for the moderate-temperature estimate of 110 °C at Quigley Soda Spring (Figure 2). To address the disconnect between low-temperature source fluid signatures and high dilation tendency on the Cross Springs Fault, it may help to examine heat flow data in the area.

Heat flow maps show a geothermal anomaly of 8 heat flow units (HFU; 334 mW/m^2) at the Sulphur Bank Mine (Figure 1), on the northwest side of the Cross Springs Fault, equivalent to a geothermal gradient of 137 °C/km (*Stimac et al.*, 2001). This anomaly drops to 4 HFU (167 mW/m^2) 5 km to the east of Sulphur Bank Mine in the vicinity of the Cross Springs Fault (*Burns*, 1996; *Stimac et al.*, 2001). We infer that the Cross Springs Fault does not allow meaningful deep fluid circulation because we would expect higher temperatures from geothermometry given the heat flow anomaly and increased geothermal gradient. The lack of apparent deep fluid circulation may be related to a change in fault geometry or lithology at depth, but this is unclear.

5.2.3 Wilbur Springs

In contrast to the BSF or the Cross Springs Fault, the Wilbur Springs area has higher fluid circulation temperatures (Figure 6). This is supported by geothermometry results, and corroborated by exploration geothermal well temperature profiles, which reached ∼175 °C at 2.1 km depth (Sunoco well, 01190003) and ∼126 °C at 1.1 km depth (Cordero-Sun well, 01190001) (Figure 2; *California Division of Oil, Gas, and Geothermal Resources*, 2024). This corresponds to shallow geothermal gradients of ∼76 °C/km to ∼98 °C/km, although more detailed thermal modeling suggests a cooler geothermal gradient of 32 °C/km in the Cordero-Sun well (cf. *Stimac et al.*, 2001). Geothermometry in the Wilbur Springs area from this study is ∼40–50 °C higher than previous estimates of 144 ± 2 °C (*Muffler*, 1978). This is because previous temperature estimates were largely based on reported well temperatures at 1,132 m depth (*Muffler*, 1978) and likely represent minimum values.

Despite high-temperature estimates from the geothermometry, some springs in the Wilbur Springs area have similar temperatures to springs along the BSF, for example, Crabtree Spring, Newman Spring, and Blank Spring (Figure 2, Table 1). We attribute this

discrepancy to mixing of meteoric fluids, cooling, and/or low flow rates, all of which reduce hot spring surface temperatures. Fluid mixing is facilitated by open and connected fracture networks, conditions which may be amplified by multiple, overprinting structural controls.

The presence of a basaltic diatreme breccia ∼1 km northeast of Wilbur Springs dated at 1.66 Ma by K–Ar (*McLaughlin et al.*, 1990) signals recent volcanism in the area and a possible local heat source as identified by heat flow studies (*Burns*, 1996). However, geophysical evidence for a shallow magma body is lacking. There is a negative gravity anomaly at Wilbur Springs, but it is interpreted to be related to a geothermal reservoir rather than a magma body because borehole temperatures at 1 km are only 140 °C (*Muffler*, 1978). The top of the gravity anomaly is located at 0.75 km depth beneath the Wilbur Springs antiform (*Harrington and Verosub*, 1981), shown schematically in Figure 11.

Highway 20 Sulfur Spring has lower geothermometry temperatures than springs to the east along the Wilbur Springs antiform, but higher than springs on the BSF or the Cross Springs Fault. This spring is located <2 km west of the synform that forms a pair with the Wilbur Springs antiform (*McLaughlin et al.*, 1990; *Mclaughlin et al.*, 2018). The location and geothermometry of Highway 20 Sulfur Spring suggest that it is sourced by fluids in a different fracture network than springs to the east along the Wilbur Springs antiform.

5.2.4 Limitations

Although our analysis emphasizes dilation tendency as a proxy for identifying permeable fault pathways, fluid flow requires more than a mechanically favorable structure. At minimum, three conditions must be met: (1) a permeable pathway, such as a critically oriented or reactivated fault; (2) a fluid source; and (3) a sufficient pressure gradient to drive flow from source to sink. Our results therefore represent only one component of this broader system. In addition, other variables such as fault or fracture roughness and rock stiffness determine whether a well-oriented fracture will open and remain open. These factors are not captured by dilation tendency analysis alone, which offers only a simplified measure of the potential for fracture opening.

Mismatches between predicted high dilation tendency and observed fluid discharge may reflect a lack of local fluid sources or insufficient pressure gradients to drive flow, or rocks with low stiffness. Conversely, springs occurring in low-T_d zones, such as along the Bartlett Springs Fault, may be sustained by elevated pore fluid pressures or focused hydraulic gradients that overcome unfavorable mechanical orientations. In addition, hot spring locations are influenced by elevated geothermal gradients associated with shallow intrusions and the magmatic history of the Clear Lake region (*McLaughlin*, 1981b); we recognize that structural controls alone do not fully explain their distribution.

Stress and permeability evolve through time; fluid flow and dilation tendency are therefore not constant, and our analysis does not represent longer-term variations in fault behavior. The area's complex deformation history, marked by successive episodes of contraction, translation, and extension, has produced overprinting folds and faults. Dilation tendency is sensitive to changes in faulting regime caused by rotations in stress orientations (Figure 9b). Older, preexisting structures may exhibit moderate to high dilation tendencies in the modern stress field and can be reactivated depending on their orientation (e.g., *Melosh et al.*, 2024b).

5.2.5 Lithological Control: Serpentinite

Serpentinite plays a dual role as both a mechanically weak rock and a low-permeability fluid barrier. Given the Coast Ranges' prolonged deformation history and the weak, low-density nature of serpentinite, these rocks can form bifurcating and elongate stringers that either align with or crosscut the structural grain. Because of its low density, serpentinite may be buoyantly emplaced in zones of transtension, such as the step-over at Lake Pillsbury (*Moore et al.*, 2018), where it can act as a fluid barrier in an otherwise structurally favorable setting for fluid flow. For these reasons, serpentinite is an important lithology to consider when developing fluid circulation models (Figure 11).

Within the core of the BSF, highly sheared serpentinite lenses occur as elongate bodies within the fault zone core down to the outcrop scale (*Mclaughlin et al.*, 2018). These serpentinite bodies act as low-permeability barriers that can obstruct or restrict fluid circulation, depending on their geometry and subsurface distribution. For example, Newman Spring is situated along a serpentinite contact that strikes approximately perpendicular to the BSF and appears to control the location of the spring (*Mclaughlin et al.*, 2018).

Serpentinite of the Coast Range ophiolite is folded between ∼2.5 and 5 km depth beneath the Wilbur Springs area (Figure 3b; *Langenheim et al.*, 2024, see their cross section 11), which is supported by the lithology encountered in well 01190003 (*California Division of Oil, Gas, and Geothermal Resources*, 2024). This deep serpentinite body may limit fluid circulation to the upper ∼5 km. A fluid circulation temperature estimate of 180–190 °C at 5 km implies a geothermal gradient of 33–36 °C/km (assuming surface water temperatures between 10 and 15 °C), similar to the estimate of *Stimac et al.* (2001) (32 °C/km).

Detrital serpentinite is also interbedded within lower Great Valley group sedimentary rocks at Wilbur Springs (Figures 2, 3), but likely has a higher porosity than sheared serpentinite lenses due to its coarse grain size and polymict detrital grains (e.g., *Wakabayashi*, 2019).

5.2.6 Dilation Tendency Uncertainties

Because dilation tendency (T_d) analyses rely on assumptions about stress magnitudes and orientations, which have inherent uncertainties and their own sets

of assumptions, a sensitivity analysis can place results within a broader range of plausible stress conditions.

Using a stress drop study from the Hayward Fault (*Lozos et al.*, 2015) to constrain stress magnitudes in this study necessarily involves assumptions, including possible differences in rupture depth, uncertainty in scaling stress drop to absolute stress magnitudes, and variability in stress orientations between distinct fault systems. Nevertheless, the Hayward Fault and the BSF share several key attributes that support the comparison: both are of similar scale, accommodate predominantly dextral strike-slip kinematics, cut through the same bedrock assemblages, and extend across comparable seismogenic depth ranges. Their spatial proximity within the northern California plate boundary system further justifies treating the Hayward Fault as a reasonable analog for bounding stress magnitudes on the Bartlett Springs Fault.

The maximum horizontal stress (S_{Hmax}) is consistently oriented northeast–southwest throughout the Coast Ranges of northern California (Figure 1; *Provost and Houston*, 2003). Although the dilation tendency analysis in this study is sensitive to variations in S_{Hmax}, regional and local differences within the study area are minimal (∼6°), resulting in only a slight decrease in average dilation tendency of 0.04. Although stress orientation estimates remain incomplete due to limited microseismic data and lack of other stress orientation data, they represent the best available constraint.

S_{Hmax} orientations are well constrained, but confidence limits vary due to differences in microseismic event density and focal mechanism variability, leading to orientation errors ranging from ∼9° to 55° (*Provost and Houston*, 2003). Accounting for these errors would introduce similar uncertainty ranges in dilation tendency estimates. However, the regional consistency of stress orientations supports the validity of using an average S_{Hmax} orientation in this study.

The maximum principal stress orientation determined by *Provost and Houston* (2003) is shallowly to moderately plunging near Wilbur Springs. The estimated angular errors at the two nearby stress inversion locations, NCA43 and NCA46, are 18.22° and 8.60°, respectively. Our sensitivity analysis shows that this angular error may impact our T_d results, either increasing or decreasing values depending on relative fault orientation (Figure 9a). However, angular uncertainties are not large enough to change the observation that northeast-striking faults have a higher dilation tendency relative to northwest-striking faults, which would require a rotation of over 100°.

The model assumes a two-dimensional framework with vertical fault dips, simplifying the true three-dimensional geometries. This is a major limitation; however, measuring fault orientation in the field is not always possible due to poor exposure. Our uncertainty analysis helps account for this limitation by quantifying some of the possible variability of dilation tendency in three dimensions (Figure 9). In strike-slip fault regimes, the sensitivity of dilation tendency implies that poorly oriented faults may have increased dilation at depth if they are dipping at angles lower than 90° or have a change in dip with depth (Figure 9b).

In addition to uncertainties in stress orientations, variations in stress magnitudes also influence dilation tendency. Variations in the relative magnitudes of the principal stresses, for example, where the vertical stress changes role in zones of tensile stress along fold hinges, can shift the stress regime and modify fault behavior (Figure 9b). In regions of low differential stress, even small changes in normal stress on a fault plane can produce large shifts in dilation tendency, amplifying the sensitivity of fault permeability to stress perturbations.

6 Conclusions

Our investigation confirms that high-temperature geothermal circulation can persist in transpressional zones through the synergistic effect of folding and fault geometry. The Wilbur Springs system demonstrates that while major strike-slip structures like the BSF may act as regional fluid barriers, active antiformal hinges provide a critical mechanism for localizing tensile stress. When these hinges are intersected by faults optimally oriented for dilation, they create a robust, deep-seated permeability network along plunging fault intersections. This multi-factor model provides a new framework for identifying geothermal resources in complex tectonic settings where surface expressions may be diverted away from primary fault traces in areas of contractional strain.

Acknowledgements

We would like to acknowledge helpful discussions and reviews by Glenn Melosh, Max Wilmarth, Vicki Langenheim, and Jared Peacock, which greatly helped improve this manuscript. We appreciate the hospitality of the staff at the Wilbur Springs Resort and access to the property to fly thermal drone imagery. We would like to thank the two reviewers, Adam Cawood and Åke Fagereng, who helped improve this manuscript. Reference in this paper to any specific commercial product, process, or service, or the use of any trade, firm or corporation name is for the information and convenience of the public, and does not constitute endorsement, recommendation, or favoring by the Department of the Interior.

Author contributions

B. L. Melosh contributed the conceptual development of the research project and hypothesis, geothermometry analysis, dilation tendency analysis, interpretations, writing, and figure creation. O. Callahan contributed drone operation, planning, data interpretation, writing, and figure creation.

Data availability

Dilation tendency data (*Melosh*, 2025) and thermal maps (*Melosh and Callahan*, 2026) from this project are available as U.S. Geological Survey data releases. Fluid geochemistry data are available from *Thompson et al.* (1981) and in this work.

Competing interests

The authors declare no competing interests.

Peer review

This publication was peer-reviewed by Adam Cawood and Åke Fagereng. The full peer-review report can be found here: Review Report.

Copyright notice

© Author(s) 2026. This article is distributed under the Creative Commons Attribution 4.0 International License, which permits unrestricted use, distribution, and reproduction in any medium, provided the original author(s) and source are credited.

References

Anderson, T. R., and J. P. Fairley (2008), Relating permeability to the structural setting of a fault-controlled hydrothermal system in southeast Oregon, USA, *Journal of Geophysical Research*, *113*(B5), https://doi.org/10.1029/2007jb004962.

Barcelona, H., D. Yagupsky, N. Vigide, and M. Senger (2019), Structural model and slip-dilation tendency analysis at the Copahue geothermal system: Inferences on the reservoir geometry, *Journal of Volcanology and Geothermal Research*, *375*, 18–31, https://doi.org/10.1016/j.jvolgeores.2019.03.007.

Burns, K. L. (1996), Heat flow and hot dry rock geothermal resources of the Clearlake Region, northern California, *Tech. rep.*, Los Alamos National Lab., NM (United States).

Caine, J. S., R. L. Bruhn, and C. B. Forster (2010), Internal structure, fault rocks, and inferences regarding deformation, fluid flow, and mineralization in the seismogenic Stillwater normal fault, Dixie Valley, Nevada, *Journal of Structural Geology*, *32*(11), 1576–1589, https://doi.org/10.1016/j.jsg.2010.03.004.

California Division of Oil, Gas, and Geothermal Resources (2024), Well finder, *https://maps . conservation. ca. gov/doggr/wellfinder (accessed February 6 2024)*.

Callahan, O., and N. Hart-Wagoner (2025), Applications and Limitations of Drone-Based Thermography in Geothermal Exploration, Characterization, and Monitoring, in *Geothermal Resources Council Transactions*, pp. 1714–1739.

Callahan, O. A., P. Eichhubl, J. E. Olson, and N. C. Davatzes (2019), Fracture mechanical properties of damaged and hydrothermally altered rocks, Dixie Valley-Stillwater fault zone, Nevada, USA, *Journal of Geophysical Research. Solid Earth*, *124*(4), 4069–4090, https://doi.org/10.1029/2018jb016708.

Constenius, K. N., R. A. Johnson, W. R. Dickinson, and T. A. Williams (2000), Tectonic evolution of the Jurassic–Cretaceous Great Valley forearc, California: Implications for the Franciscan thrust-wedge hypothesis, *Geological Society of America Bulletin*, *112*(11), 1703–1723, https://doi.org/10.1130/0016-7606(2000)112<1703:teotjc>2.0.co;2.

Curewitz, D., and J. A. Karson (1997), Structural settings of hydrothermal outflow: Fracture permeability maintained by fault propagation and interaction, *Journal of Volcanology and Geothermal Research*, *79*(3-4), 149–168, https://doi.org/10.1016/s0377-0273(97)00027-9.

Cyr, A. J. (2013), Using 10 Be erosion rates and fluvial channel morphology to constrain fault throw rates in the southwestern Sacramento River Valley, California, USA, in *AGU Fall Meeting Abstracts*, vol. 2013, pp. EP53A–0732.

Esri (2015), ArcGIS, https://www.arcgis.com/home/item.html?id=1b243539f4514b6ba35e7d995890db1d, accessed: 2026-10-25.

Evans, M. A., and M. P. Fischer (2012), On the distribution of fluids in folds: A review of controlling factors and processes, *Journal of Structural Geology*, *44*, 2–24, https://doi.org/10.1016/j.jsg.2012.08.003.

Faulds, J., and N. Hinz (2014), Favorable tectonic and structural settings of geothermal systems in the Great Basin region, western USA: Proxies for discovering blind geothermal systems, in *Proceedings World Geothermal Congress 2015*.

Faulds, J. E., C. D. Henry, and N. H. Hinz (2005), Kinematics of the northern Walker Lane: An incipient transform fault along the Pacific–North American plate boundary, *Geology*, *33*(6), 505, https://doi.org/10.1130/g21274.1.

Ferrill, D., J. Winterle, G. Wittmeyer, D. Sims, S. Colton, and A. Armstrong (1999), Stressed rock strains groundwater at yucca mountain, Nevada, *GSA Today*, *9*(5), 1–8.

Ferrill, D. A., K. J. Smart, and A. P. Morris (2020), Fault failure modes, deformation mechanisms, dilation tendency, slip tendency, and conduits v. seals, *Geological Society Special Publication*, *496*(1), 75–98, https://doi.org/10.1144/sp496-2019-7.

Fournier, R., and R. Potter (1982), Revised and expanded silica (quartz) geothermometer, *Bull. , Geotherm. Resour. Counc. ; (United States)*, *11:10*.

Gaines, J. (2008), Fluvial strath terrace formation and soil development with tectonic implications along Cache Creek, California, *Masters Thesis, Humbolt State University, 113p.*

Giggenbach, W. F. (1984), Mass transfer in hydrothermal alteration systems, *Geochimica et cosmochimica acta*, pp. 2693–2711.

Giggenbach, W. F. (1986), Graphical techniques for the evaluation of water/rock equilibration conditions by use of Na, K, Mg and Ca contents of discharge waters, in *Proc. 8th New Zealand Geothermal Workshop*, pp. 37–44.

Giggenbach, W. F. (1988), Geothermal solute equilibria. Derivation of Na-K-Mg-Ca geoindicators, *Geochimica et cosmochimica acta*, *52*(12), 2749–2765, https://doi.org/10.1016/0016-7037(88)90143-3.

Harrington, J. M., and K. L. Verosub (1981), A detailed gravity survey of the Wilbur Springs area, *Tech. rep.*, US Geological Survey.

Irujo, P. G. (2022), IRimage: open-source software for processing images from infrared thermal cameras, *PeerJ. Computer Science*, *8*, e977.

Langenheim, V. E., R. J. McLaughlin, and B. L. Melosh (2024), Integrated geologic and geophysical modeling across the Bartlett Springs fault zone, northern California (USA): Implications for fault creep and regional structure, *Geosphere*, *20*(1), 129–151, https://doi.org/10.1130/ges02684.1.

Lawton, J. E. (1956), Geology of the north half of the Morgan Valley quadrangle and the south half of the Wilbur Springs quadrangle, Ph.D. thesis, Stanford University, Stanford, USA.

Libbey, R. B., A. E. Williams-Jones, B. L. Melosh., and N. R. Backeberg (2015), Characterization of geothermal activity along the North American–Caribbean Plate boundary in Guatemala: The Joaquina geothermal field, *Geothermics*, *56*, 17–34, https://doi.org/10.1016/j.geothermics.2015.03.002.

Lienkaemper, J., S. DeLong, R. Mcpherson, J. Mielke, N. Avdievitch, A. Pickering, and C. Lloyd (2014), Characterizing recent slip on the kuikui fault, a link between the Green Valley and Bartlett Springs fault zones, Wilson valley, northern California, in *AGU Fall meeting*.

Lienkaemper, J. J. (2010), Recently active traces of the Bartlett Springs Fault, California: A digital database, https://doi.org/10.3133/ds541.

Lozos, J. C., R. A. Harris, J. R. Murray, and J. J. Lienkaemper (2015), Dynamic rupture models of earthquakes on the Bartlett Springs Fault, Northern California: BARTLETT SPRINGS FAULT EARTHQUAKE MODELS, *Geophysical Research Letters*, *42*(11), 4343–4349, https://doi.org/10.1002/2015gl063802.

Maffucci, R., S. Corrado, L. Aldega, S. Bigi, A. Chiodi, L. Di Paolo, G. Giordano, and C. Invernizzi (2016), Cap rock efficiency of geothermal systems in fold-and-thrust belts: Evidence from paleo-thermal and structural analyses in Rosario de La Frontera geothermal area (NW Argentina), *Journal of Volcanology and Geothermal Research*, *328*, 84–95, https://doi.org/10.1016/j.jvolgeores.2016.10.008.

McLaughlin, R. J. (1981a), Tectonic setting of pre-Tertiary rocks and its relation to geothermal resources in The Geysers-Clear Lake area, *U.S. Geological Survey Professional Paper*, *1141*, 3–23.

McLaughlin, R. J. (1981b), Research in the Geysers-Clear Lake geothermal area, northern California, *Tech. rep.*, US geological Survey, https://doi.org/10.2172/6673597.

McLaughlin, R. J., H. N. Ohlin, D. J. Thormahlen, D. L. Jones, J. W. Miller, and C. D. Blome (1990), Geologic Map and Structure sections of the Little Indian Valley-Wilbur Springs Geothermal area, *Northern Coast Ranges, California: US Geological Survey Miscellaneous Investigation Series Map I-1706, 1:24,000*.

Mclaughlin, R. J., C. Barry, C. S. Moring, and Z. C. Hitchcock (2018), Framework geologic map and structure sections along the Bartlett Springs fault zone and adjacent area from Round Valley to Wilbur Springs, northern Coast Ranges, California, *Tech. rep.*, US Geological Survey, https://doi.org/10.3133/sim3395.

Melosh, B. (2026), Stepovers and beyond: Structural controls of the geysers geothermal system and the broader Clear Lake region, in *Proceedings, 51st Workshop on Geothermal Reservoir Engineering, Stanford University*.

Melosh, B. L. (2025), Dilation and slip tendency for a portion of the Southern Bartlett Springs fault and surrounding fault zones in the Wilbur Springs area, Northern California Coast Ranges, *U. S. Geological Survey, Data Release*.

Melosh, B. L., and O. Callahan (2026), Processed sUAS products from Sulphur Creek near Wilbur Hot Springs, northern California Coast Ranges, https://doi.org/10.5066/P1E4XWLQ.

Melosh, B. L., and V. E. Langenheim (2022), Serpentinite bodies and complex fault geometry through time: the southern Bartlett Springs fault, northern California Coast Ranges, *AGU Fall Meeting*.

Melosh, B. L., C. D. Rowe, C. Gerbi, C. E. Bate, and D. Shulman (2016), The spin zone: Transient mid-crust permeability caused by coseismic brecciation, *Journal of Structural Geology*, *87*, 47–63, https://doi.org/10.1016/j.jsg.2016.04.003.

Melosh, B. L., J. Bodtker, and Z. Valin (2024a), Geologic map and structure sections along the southern part of the Bartlett Springs Fault Zone and adjacent areas from Cache Creek to Lake Berryessa, northern Coast Ranges, California, *U. S. Geological Survey Scientific Investigations Map 3514, 2 sheets, scale 1:24,000, 20 p. pamphlet*.

Melosh, B. L., R. J. McLaughlin, and H. N. Ohlin (2024b), The geometry of fault reactivation and uplift along the central part of the Maacama Fault Zone, Northern California Coast Ranges (USA), *Geosphere*, *20*(6), 1511–1532, https://doi.org/10.1130/ges02750.1.

Moore, D. E., R. J. McLaughlin, and J. J. Lienkaemper (2018), Serpentinite-rich gouge in a creeping segment of the Bartlett Springs Fault, northern California: Comparison with SAFOD and implications for seismic hazard, *Tectonics*, *37*(12), 4515–4534, https://doi.org/10.1029/2018tc005307.

Muffler, L. J. P. (1978), Assessment of geothermal resources of the United States, *U. S. Geological Survey Circular 790*.

Muraoka, H., M. Takahashi, H. Sundhoro, S. Dwipa, Y. Soeda, M. Momita, and K. Shimada (2010), Geothermal systems constrained by the Sumatran fault and its pull-apart basins in Sumatra, western Indonesia, in *Proceedings World Geothermal Congress 2010*, pp. 1–9.

Nicholson, K. (1993), Geothermal Systems, in *Geothermal Fluids*, pp. 1–18, Springer Berlin Heidelberg, Berlin, Heidelberg, https://doi.org/10.1007/978-3-642-77844-5_1.

Nitschke, F., S. Held, T. Neumann, and T. Kohl (2018), Geochemical characterization of the Villarrica geothermal system, Southern Chile, part II: Site-specific re-evaluation of SiO2 and Na-K solute geothermometers, *Geothermics*, *74*, 217–225, https://doi.org/10.1016/j.geothermics.2018.03.006.

Pluhar, C., R. Coe, J. Lewis, F. Monastero, and J. Glen (2006), Fault block kinematics at a releasing stepover of the Eastern California shear zone: Partitioning of rotation style in and around the Coso geothermal area and nascent metamorphic core complex, *Earth and Planetary Science Letters*, *250*(1-2), 134–163, https://doi.org/10.1016/j.epsl.2006.07.034.

Powell, T., and W. Cumming (2010), Spreadsheets for geothermal water and gas geochemistry, in *Thirty-Fifth Workshop on Geothermal Reservoir Engineering*, pp. 408–417.

Prescott, W. H., J. C. Savage, J. L. Svarc, and D. Manaker (2001), Deformation across the Pacific-North America plate boundary near San Francisco, California, *Journal of Geophysical Research*, *106*(B4), 6673–6682, https://doi.org/10.1029/2000jb900397.

Provost, A.-S., and H. Houston (2003), Stress orientations in northern and central California: Evidence for the evolution of frictional strength along the San Andreas plate boundary system: STRENGTH OF THE SAN ANDREAS FAULT SYSTEM, *Journal of Geophysical Research*, *108*(B3), https://doi.org/10.1029/2001jb001123.

Robert, F., and K. H. Poulsen (2001), Vein formation and deformation in Greenstone gold deposits, in *Structural Controls on Ore Genesis*, vol. 14, edited by J. P. Richards and R. M. Tosdal, pp. 111–155, Society of Economic Geologists, https://doi.org/10.5382/rev.14.05.

Romano, P., and M. Liotta (2020), Using and abusing Giggenbach ternary Na-K-Mg diagram, *Chemical Geology*, *541*(119577), 119,577, https://doi.org/10.1016/j.chemgeo.2020.119577.

Rowland, J. V., and R. H. Sibson (2004), Structural controls on hydrothermal flow in a segmented rift system, Taupo Volcanic Zone, New Zealand, *Geofluids*, *4*(4), 259–283, https://doi.org/10.1111/j.1468-8123.2004.00091.x.

Schmitt, A. K., M. Grove, T. M. Harrison, O. Lovera, J. Hulen, and M. Walters (2003), The Geysers-Cobb Mountain Magma System, California (Part 2): timescales of pluton emplacement and implications for its thermal history, *Geochimica et cosmochimica acta*, *67*(18), 3443–3458, https://doi.org/10.1016/s0016-7037(03)00126-1.

Sibson, R. H. (1994), Crustal stress, faulting and fluid flow, *Geological Society Special Publication*, *78*(1), 69–84, https://doi.org/10.1144/gsl.sp.1994.078.01.07.

Sibson, R. H. (1996), Structural permeability of fluid-driven fault-fracture meshes, *Journal of Structural Geology*, *18*(8), 1031–1042, https://doi.org/10.1016/0191-8141(96)00032-6.

Sibson, R. H., F. Robert, and K. H. Poulsen (1988), High-angle reverse faults, fluid-pressure cycling, and mesothermal gold-quartz deposits, *Geology*, *16*(6), 551, https://doi.org/10.1130/0091-7613(1988)016<0551:harffp>2.3.co;2.

Siler, D. L. (2023), Structural discontinuities and their control on hydrothermal systems in the Great Basin, USA, *Geoenergy*, *1*(1), geoenergy2023–009, https://doi.org/10.1144/geoenergy2023-009.

Siler, D. L., N. H. Hinz, and J. E. Faulds (2018), Stress concentrations at structural discontinuities in active fault zones in the western United States: Implications for permeability and fluid flow in geothermal fields, *Geological Society of America Bulletin*, *130*(7-8), 1273–1288, https://doi.org/10.1130/b31729.1.

Stanley, W. D., H. M. Benz, M. A. Walters, and B. D. Rodriguez (1997), Tectonic controls on magmatism and geothermal resources in the Geysers-Clear Lake region, California: Integration of new geologic, earthquake tomography, seismicity, gravity, and magnetotelluric data, *Tech. rep.*, U.S. Geological Survey.

Stanley, W. D., H. M. Benz, M. A. Walters, A. Villaseñor, and B. D. Rodriguez (1998), Tectonic controls on magmatism in The Geysers–Clear Lake region: Evidence from new geophysical models, *Geological Society of America Bulletin*, *110*(9), 1193–1207, https://doi.org/10.1130/0016-7606(1998)110<1193:tcomit>2.3.co;2.

Stimac, J. A., F. Goff, and K. Wohletz (2001), Thermal modeling of the Clear Lake magmatic-hydrothermal system, California, USA, *Geothermics*, *30*(2-3), 349–390, https://doi.org/10.1016/s0375-6505(00)00062-6.

Thompson, J. M., F. E. Goff, and J. M. Donnelly-Nolan (1981), Chemical analyses of waters from springs and wells in the Clear Lake Volcanic Area, in Research in the Geysers-Clear Lake geothermal area, Northern California, eds. Robert J. McLaughlin and Julie Donnelly-Nolan, *U. S. Geological Survey, Professional Paper 1141*, pp. 183–192.

Trexler, C. C., A. E. Morelan, R. Catchings, M. Goldman, and J. Willard (2022), Evidence of active Quaternary deformation on the Great Valley fault system near Winters, northern California, *The Seismic Record*, *2*(4), 248–259, https://doi.org/10.1785/0320220029.

Unruh, J. R., B. A. Loewen, and E. M. Moores (1995), Progressive arcward contraction of a Mesozoic-Tertiary fore-arc basin, southwestern Sacramento Valley, California, *Geological Society of America Bulletin*, *107*(1), 38, https://doi.org/10.1130/0016-7606(1995)107<0038:pacoam>2.3.co;2.

U.S. Geological Survey (2004), Quaternary Fault and Fold Database for the Nation, https://pubs.usgs.gov/fs/2004/3033/fs-2004-3033.html, accessed: 2026-11-19.

U.S. Geological Survey (2018), 1-meter Digital Elevation Models (DEMs), *USGS National Map 3DEP Downloadable Data Collection: U. S. Geological Survey. Accessed February 2022.*

U.S. Geological Survey (2026), 3D Elevation Program (3DEP) Lidar Point Cloud.

Verma, M. P. (2000), Chemical thermodynamics of silica: a critique on its geothermometer, *Geothermics*, *29*(3), 323–346, https://doi.org/10.1016/s0375-6505(99)00064-4.

Wakabayashi, J. (2019), Sedimentary compared to tectonically-deformed serpentinites and tectonic serpentinite mélanges at outcrop to petrographic scales: Unambiguous and disputed examples from California, *Gondwana Research: International Geoscience Journal*, *74*, 51–67, https://doi.org/10.1016/j.gr.2019.04.005.

Wentworth, C. M., M. C. Blake, Jr, D. L. Jones, A. W. Walter, and M. D. Zoback (1984), Tectonic wedging associated with emplacement of the Franciscan assemblage, California Coast Ranges, in *Franciscan Geology of Northern California: Pacific Section SEPM*, vol. 43, edited by M. Clark Blake, Jr, pp. 163–173, Pacific Section Soc. Economic Paleontologists and Mineralogists.

Zeng, Y., and Z.-K. Shen (2014), Fault network modeling of crustal deformation in California constrained using GPS and geologic observations, *Tectonophysics*, *612-613*, 1–17, https://doi.org/10.1016/j.tecto.2013.11.030.